



Optimal RWIS Sensor Density and Location – Phase III:
**Continuous Mapping of Winter Road Surface
Conditions via Big Data and Deep Learning**

<http://aurora-program.org>

Aurora Project 2019-01

**Final Report
August 2021**

About Aurora

The Aurora program is a partnership of highway agencies that collaborate on research, development, and deployment of road weather information to improve the efficiency, safety, and reliability of surface transportation. The program is administered by the Center for Weather Impacts on Mobility and Safety (CWIMS), which is housed under the Institute for Transportation at Iowa State University. The mission of Aurora and its members is to seek to implement advanced road weather information systems (RWIS) that fully integrate state-of-the-art roadway and weather forecasting technologies with coordinated, multi-agency weather monitoring infrastructures.

Iowa State University Nondiscrimination Statement

Iowa State University does not discriminate on the basis of race, color, age, ethnicity, religion, national origin, pregnancy, sexual orientation, gender identity, genetic information, sex, marital status, disability, or status as a US veteran. Inquiries regarding nondiscrimination policies may be directed to the Office of Equal Opportunity, 3410 Beardshear Hall, 515 Morrill Road, Ames, Iowa 50011, telephone: 515-294-7612, hotline: 515-294-1222, email: eooffice@iastate.edu.

Disclaimer Notice

The contents of this report reflect the views of the authors, who are responsible for the facts and the accuracy of the information presented herein. The opinions, findings and conclusions expressed in this publication are those of the authors and not necessarily those of the sponsors.

This document is disseminated under the sponsorship of the U.S. Department of Transportation in the interest of information exchange. The U.S. Government assumes no liability for the use of the information contained in this document. This report does not constitute a standard, specification, or regulation.

The U.S. Government does not endorse products or manufacturers. If trademarks or manufacturers' names appear in this report, it is only because they are considered essential to the objective of the document.

Quality Assurance Statement

The Federal Highway Administration (FHWA) provides high-quality information to serve Government, industry, and the public in a manner that promotes public understanding. Standards and policies are used to ensure and maximize the quality, objectivity, utility, and integrity of its information. The FHWA periodically reviews quality issues and adjusts its programs and processes to ensure continuous quality improvement.

Iowa DOT Statements

Federal and state laws prohibit employment and/or public accommodation discrimination on the basis of age, color, creed, disability, gender identity, national origin, pregnancy, race, religion, sex, sexual orientation or veteran's status. If you believe you have been discriminated against, please contact the Iowa Civil Rights Commission at 800-457-4416 or the Iowa Department of Transportation affirmative action officer. If you need accommodations because of a disability to access the Iowa Department of Transportation's services, contact the agency's affirmative action officer at 800-262-0003.

The preparation of this report was financed in part through funds provided by the Iowa Department of Transportation through its "Second Revised Agreement for the Management of Research Conducted by Iowa State University for the Iowa Department of Transportation" and its amendments.

The opinions, findings, and conclusions expressed in this publication are those of the authors and not necessarily those of the Iowa Department of Transportation or the U.S. Department of Transportation Federal Highway Administration.

Technical Report Documentation Page

1. Report No. Aurora Project 2019-01	2. Government Accession No.	3. Recipient's Catalog No.	
4. Title and Subtitle Optimal RWIS Sensor Density and Location – Phase III: Continuous Mapping of Winter Road Surface Conditions via Big Data and Deep Learning	5. Report Date August 2021		6. Performing Organization Code InTrans Project 19-156
	8. Performing Organization Report No.		
7. Author(s) Mingjian Wu, Tae J. Kwon, and Liping Fu	10. Work Unit No. (TRAVIS)		
9. Performing Organization Name and Address Department of Civil & Environmental Engineering, University of Alberta 9211-116 Street NW Edmonton, Alberta, Canada T6G 1H9	11. Contract or Grant No. Federal SPR Part II, CFDA 20.205		
	13. Type of Report and Period Covered Final Report		
12. Sponsoring Organization Name and Address Aurora Program Iowa Department of Transportation 800 Lincoln Way Ames, Iowa 50010	Federal Highway Administration U.S. Department of Transportation 1200 New Jersey Avenue, SE Washington, DC 20590	14. Sponsoring Agency Code TPF-5(290) SPR-3(042)	
		15. Supplementary Notes Visit https://aurora-program.org/ and https://intrans.iastate.edu/ for color pdfs of this and other research reports.	
16. Abstract <p>Road weather information systems (RWIS) have long been regarded as one of the most advanced technologies for monitoring road surface conditions (RSCs) during the winter season. While RWIS provide information essential for winter road maintenance (WRM) services, they can only be implemented at select areas largely due to budgetary constraints. It is therefore indispensable to fill large spatial gaps that exist between RWIS stations to promote safer driving conditions and lower the cost of WRM activities. Furthermore, most RWIS stations nowadays are equipped with cameras that provide users with a direct view of the road conditions being covered; however, checking RSCs via these cameras is still being done manually, which hinders the full utilization of the rich image-based road condition data.</p> <p>To help tackle these challenges, this project aimed to develop a systematic, yet transferrable, method for estimating key RSC variables (i.e., road surface temperature and slipperiness) between RWIS stations using large-scale data and two advanced modeling techniques—kriging and deep learning (DL). Road surface temperatures, dash camera images, and remotely sensed data collected along selected Iowa interstate highway segments between October 2018 and April 2019 were used to develop the models for estimating RSCs. A total of 262 hourly events and more than 10,000 images were processed and utilized for model development.</p> <p>The findings suggest that the proposed kriging method is able to capture the general RSC pattern along the highway stretch with as few as one RWIS input. In addition, the DL model developed in this study showed promising performance in automatically classifying dash camera images. The road condition images labeled by the DL model were later used for road slipperiness estimations between existing RWIS stations. Although additional data sets would be required to further confirm the validity of the developed models and the conclusiveness of the results documented herein, the proposed method will undoubtedly provide decision makers with a tool that helps to implement WRM activities more quickly, efficiently, and cost effectively.</p>			
17. Key Words big data—deep learning—geostatistics—road surface conditions—road weather information systems—RWIS—winter weather events		18. Distribution Statement No restrictions.	
19. Security Classification (of this report) Unclassified.	20. Security Classification (of this page) Unclassified.	21. No. of Pages 76	22. Price NA

OPTIMAL RWIS SENSOR DENSITY AND LOCATION – PHASE III: CONTINUOUS MAPPING OF WINTER ROAD SURFACE CONDITIONS VIA BIG DATA AND DEEP LEARNING

**Final Report
August 2021**

Principal Investigator
Tae J. Kwon, Assistant Professor
University of Alberta

Authors
Mingjian Wu, Tae J. Kwon, and Liping Fu

Sponsored by
Federal Highway Administration Aurora Program
Transportation Pooled Fund
(TPF-5(290))

Preparation of this report was financed in part
through funds provided by the Iowa Department of Transportation
through its Research Management Agreement with the
Institute for Transportation

A report from
Aurora Program
Institute for Transportation
Iowa State University
2711 South Loop Drive, Suite 4700
Ames, IA 50010-8664
Phone: 515-294-8103 / Fax: 515-294-0467
<https://aurora-program.org/> and <https://intrans.iastate.edu/>

TABLE OF CONTENTS

ACKNOWLEDGMENTS	vii
LIST OF ABBREVIATIONS AND ACRONYMS	viii
EXECUTIVE SUMMARY	ix
1. INTRODUCTION	1
1.1 Background	1
1.2 Road Weather Information Systems	2
1.3 Current Practice of Winter Road Surface Conditions Estimations	5
1.4 Research Objectives	6
2. METHODOLOGY	7
2.1 Regression Kriging	8
2.1.1 The Idea	8
2.1.2 Quantifying Spatial Structures via Semivariogram	10
2.1.3 Implementation and Evaluation	12
2.1.4 Weather Events Characterization via Nugget-to-Sill Ratio	13
2.2 Deep Learning	14
2.2.1 The Idea	14
2.2.2 Implementation and Evaluation	15
3. STUDY AREA AND DATA	17
3.1 Study Area	17
3.2 Data Description and Integration	18
3.2.1 Road Surface Temperatures and Dash Camera Images	18
3.2.2 Digital Elevation Model	20
3.2.3 Meteorological Data	20
4. RESULTS AND DISCUSSION	23
4.1 Spatial Mapping of Road Surface Temperatures	23
4.2 Spatial Mapping of Road Surface Indices	27
4.2.1 Road Surface Condition Image Recognition via Deep Learning	27
4.2.2 Road Surface Index Conversion	29
4.2.3 Road Surface Index Interpolation	31
4.3 Weather Events Characterization	34
4.3.1 Wind	34
4.3.2 Rainfall	35
5. CONCLUSION AND RECOMMENDATIONS	37
6. REFERENCES	39
APPENDIX A. RESULTS OF SPATIAL MAPPING OF ROAD SURFACE TEMPERATURE	43
APPENDIX B. RESULTS OF SPATIAL MAPPING OF ROAD SURFACE INDEX	63

LIST OF FIGURES

Figure 1-1. Typical stationary RWIS	3
Figure 1-2. Mobile RWIS unit equipped with spectral road surface temperature sensors	4
Figure 2-1. Workflow of the proposed framework	8
Figure 2-2. Example of a regression kriging process	10
Figure 2-3. A semivariogram and its associated parameters	11
Figure 2-4. Sample semivariograms of different spatial dependence classes	14
Figure 2-5. Generic architecture of a DL model for image classification	15
Figure 3-1. Study area - southern section of I-35 in Iowa	17
Figure 3-2. Web-based manual image classifier	19
Figure 3-3. Statistics of labeled RSC images	19
Figure 3-4. Data preparation. example of rainfall intensity (left) with elevations (right)	20
Figure 4-1. Examples of the RK estimated RST versus observed RST	26
Figure 4-2. Example of the interactive web visualization tool for RST	27
Figure 4-3. Deep learning model performance	28
Figure 4-4. Example of image cropping and thresholding process	30
Figure 4-5. Examples of the RK estimated RSI versus observed RSI	32
Figure 4-6. Example of the interactive web visualization tool for RSI	33
Figure 4-7. Relationship between spatial dependence and wind-related factors	35
Figure 4-8. Relationship between spatial dependence and rainfall intensity	36

LIST OF TABLES

Table 2-1. Commonly used theoretical semivariogram models	12
Table 3-1. Definition of different RSC categories	18
Table 3-2. Descriptive statistics of hourly AVL observation	20
Table 3-3. Descriptive statistics of hourly meteorological factors	21
Table 4-1. Examples of fitted trend models involved in RK for RST	23
Table 4-2. Examples of the fitted semivariogram models for RST	24
Table 4-3. RSC categories and corresponding RSI values	29
Table 4-4. Examples of trend removal results involved in RK for RSI	31
Table 4-5. Examples of the fitted semivariogram models for RSI	31
Table A-1. Fitted trend models involved in RK for RST	43
Table A-2. Fitted semivariogram models for RST	49
Table A-3. All cross validation results for RST	55
Table B-1. Fitted trend models involved in RK for RSI in 2019	63
Table B-2. Fitted semivariogram models for RSI in 2019	64
Table B-3. All cross validation results for RSI in 2019	65

ACKNOWLEDGMENTS

This research was conducted under the Federal Highway Administration (FHWA) Transportation Pooled Fund Aurora Program. The authors would like to acknowledge the FHWA, the Aurora Program partners, and the Iowa Department of Transportation (DOT), which is the lead state for the program, for their financial support and technical assistance.

Much of the work presented in this report is either accepted, published, or under-review for publication with various transportation engineering journals and conferences as follows.

Peer-Reviewed Conference Papers and Presentations (Presented or Accepted for Upcoming)

- Wu, M., T. J. Kwon, and L. Fu. 2021. Spatial Mapping of Winter Road Surface Conditions via Hybrid Geostatistical Techniques. 100th Annual Meeting of the Transportation Research Board, January 5–29, Washington, DC.
- . 2022. A Comparison of Deep Learning Models for Determining Road Surface Conditions using In-Vehicle Camera Images (Abstract). XVIth World Winter Service and Road Resilience Congress, February 7–11, Calgary.
- . 2022. Spatial Mapping of Winter Road Surface Conditions via Deep Learning and Geostatistical Techniques (Abstract). XVIth World Winter Service and Road Resilience Congress, February 7–11, Calgary.

Book Chapter

- Wu, M., T. J. Kwon, L. Fu, and A. Wong. 2021. Winter Road Weather and Surface Conditions Estimations using Intelligent Transportation System Sensors – Case Studies in North America. In *The Rise of Smart Cities: Advanced Structural Sensing and Monitoring Systems*. Elsevier Science. Accepted for publication, July 2021.

Peer-Reviewed Journal Publications (Under Review)

- Wu, M., T. J. Kwon, and L. Fu. 2021. Spatial Mapping of Winter Road Surface Conditions via Hybrid Geostatistical Techniques. Submitted to *Journal of Cold Region Engineering*.

LIST OF ABBREVIATIONS AND ACRONYMS

ANN	artificial neural network
API	application programming interface
ASE	average standard error
AT	air temperature
AVL	automated vehicle location
CSV	comma-separated values
CWS	re-Calculated directional Wind Speed
DEM	digital elevation model
DL	deep learning
DNN	deep neural network
DOT	department of transportation
ESS	environmental sensor stations
FFS	free flow speed
FHWA	Federal Highway Administration
FNR	false negative rate
FPR	false positive rate
GB	gigabyte
GIS	geographic information system
GLS	generalized least squares
GPS	global positioning system
GPU	graphics processing unit
HTML	HyperText Markup Language
IEM	Iowa Environmental Mesonet
ITS	intelligent transportation system
MAE	mean absolute error
MLR	multiple linear regression
NSR	nugget-to-sill ratio
OK	ordinary kriging
OLS	ordinary least squares
RF	random forest
RGB	red-green-blue
RK	regression kriging
RMSE	root mean square error
RMSSE	root mean square standardized error
RPU	remote processing unit
RSC	road surface condition
RSI	road surface index
RST	road surface temperature
RWIS	road weather information system
SK	simple kriging
SVM	support vector machine
TM	thermal mapping
WD	wind direction (degrees from the north-south direction)
WRM	winter road maintenance
WS	wind speed

EXECUTIVE SUMMARY

The monitoring and estimations of road surface conditions (RSCs) play a critical role in optimizing winter road maintenance (WRM) activities. In recent decades, road weather information systems (RWIS), in both stationary and mobile, have gained popularity with many road maintenance authorities and become a predominant intelligent transportation system (ITS) technology. While RWIS provide real-time and near-future RSC information that is critical in making timely maintenance related decisions, RWIS are relatively expensive to maintain and operate and are therefore only installed at a limited number of locations.

The limited number of RWIS stations along with the need to monitor spatially large road networks with vastly varied conditions necessitate a strategic and scientific approach to the continuous and accurate monitoring of RSCs during inclement weather events. Furthermore, most RWIS stations nowadays are equipped with cameras that provide users with a direct view of the RSCs; however, the process of classifying RSCs using these camera images is still being done manually. If this process can be automated, transportation agencies will be able to use the rich image-based road condition data more effectively and, in turn, improve the level of service that they provide.

To tackle the foregoing challenges and provide solutions to better serve the public and road authorities, this project aimed to develop a methodological framework for estimating winter RSCs and to automate the process of image recognition to fill in the spatial gap of unmonitored areas using RWIS and other sensing technologies.

To evaluate the feasibility and reliability of the proposed methods, a case study was conducted by selecting several highway segments from Iowa, where a comprehensive geodatabase was constructed by incorporating the historical observations of RSC variables, weather conditions, and vehicle-mounted dash camera images collected by the Iowa automated vehicle location (AVL) system from October 2018 through April 2019, as well as the geographical and topographical features of each highway stretch.

As a result, a hybrid geostatistical model, regression kriging (RK), was developed by incorporating two conceptually different models to map spatial variability and strengthen the explanatory power of key RSC variables, which included the road surface temperature (RST) and road surface index (RSI), representing road slipperiness.

Semivariogram modeling was also involved in the RK to investigate the spatial variations of target variables. In total, the researchers developed 228 and 34 semivariogram models for RST and RSI, respectively. These two variables were also utilized to evaluate the feasibility of RK by conducting cross validations.

By using the results from the case study, the researchers observed that RK is both reliable and capable in estimating both RST and RSI in the unmonitored regions between RWIS stations. However, the estimation quality is somewhat dependent on the density of the RWIS network.

When the number of point measurements increases, the estimation accuracy increases with it. Regardless, with as little as one point measurement as input, RK can well mimic the general pattern of the RSC variables along a stretch of highway.

A deep learning (DL) model was developed to automate the process of RSC image recognition. The developed DL model was shown to be highly accurate with training and validation accuracies being 99.89% and 94.62%, respectively. The confusion matrix, which shows the performance of the DL model in terms of both false positive and false negative measures, also affirmed that the model can successfully distinguish between the different RSC categories. The validation accuracy for each category was over 90%, suggesting that the DL model is a practically applicable approach for determining RSC from dash camera images.

As previously mentioned, RSI was one of the RSC variables that were used in the development of the RK method. It is a friction-like surrogate measure used as a numerical indicator for the overall RSC. RSI itself is not directly collected at the AVL, but is instead converted from the RSC category classified by the trained DL model prior to RK interpolation. To make the converted RSI more representative, an image thresholding technique was used to further adjust the RSI values for images labeled with the same RSC category. Converted RSI values were then used as input in the RK method for RSI interpolation.

In addition to estimating RSC variables, it is also important to understand the relationship between spatial variation patterns of the variables and the underlying meteorological factors, which can be used as priori knowledge or fingerprints for implementing RK without the need to send personnel to collect data before making decisions on WRM activities.

The nugget-to-sill ratio (NSR) obtained from the semivariogram model of a target variable represents the spatial dependence of the variable and, therefore, can be used to characterize the spatial dependence of the RSC. This NSR value can vary depending on the weather event. Based on the literature review and other available data, wind and rainfall were used in this study to examine potential correlations between RST and wind and rainfall weather events. All variables relating to wind and rainfall were aggregated into the three NSR classes (i.e., spatial dependence classes). Due to the lack of data, an analysis pertaining to RST was only included in this portion of the analysis. Overall, strong wind and heavy rainfall tended to create a stronger spatial dependence of RST in the study area.

Finally, the developed solutions were integrated into a HyperText Markup Language (HTML) based visualization application to demonstrate the robustness of the proposed method and the resulting estimations between RWIS stations.

1. INTRODUCTION

1.1 Background

Intelligent transportation system (ITS) technology is an important advancement in modern transportation engineering that has played a crucial role in improving traffic safety and mobility. For cold regions that experience severe weather conditions, the improvements that ITS technology brings is even more significant. Within these cold regions, there is often frequent snow, sleet, ice, and frost events. And, depending on the intensity of the precipitation, it results in different kinds of road surface conditions (RSCs). If the intensity of precipitation is great, RSCs are likely to be poor, resulting in unsafe driving conditions that make drivers more prone to crashes, which are statistically far more common in the winter season.

According to studies sponsored by the Federal Highway Administration (FHWA), about 21% of all crashes each year are weather-related. Among these crashes, 5,000 people are killed and more than 418,000 people are injured each year (FHWA 2020). In another study, conducted by the Ministry of Transportation–Ontario (MTO), its Ontario Road Safety Annual Reports (1993–2009) revealed that due to wet or snowy and icy road surface conditions, the total number of vehicle crashes has increased by about 17% over the last 16 years. Other than road surface conditions, snow accumulation and wind-blown debris also pose problems for motorists. These create hazardous road conditions that lead to reduced road capacity, decreased traffic mobility, and road closures (Goodwin and Pisano 2004).

The effect of snow events on road performance is a topic that has been backed up by formal research. Agarwal et al. (2005) found that, depending on the intensity of the snow event, the capacity and average vehicle operating speed can decrease by 4.29 to 22.43% and 4.17 to 13.46%, respectively (Agarwal et al. 2005). Kwon et al. (2013) conducted a similar yet more comprehensive empirical investigation on the effects of inclement weather on highway capacity and free flow speed (FFS), where the researchers found that snow-covered road surface conditions could reduce capacity and FFS by 44.24% and 17.01%, respectively.

Given the poor track record with winter weather incidents, transportation agencies strive to provide the most optimal driving conditions through the use of various winter road maintenance (WRM) operations. These activities include plowing, deicing, and sanding operations that aim to reduce the severity and odds of crashes by mechanically removing snow and ice from the road, as well as applying abrasives to increase vehicle traction. However, due the uncertain nature of weather events and the expansive spatial distance covered by most highway networks, it becomes very difficult for transportation agencies to monitor and predict RSCs, which in turn makes both planning for WRM operations and providing accurate RSC information to the general public quite challenging.

For transportation agencies to prevent or at least reduce the number of weather-related road incidents, staff must first be able to make timely and well-informed decisions regarding their WRM operations. If they are unable to do so, it substantially increases the financial burden of

these operations as, by nature, WRM operations are very costly due to their reliance on heavy machinery and significant manpower demands. It is estimated that North America as a whole spends roughly \$2.3 billion (US dollars) annually on WRM maintenance operations (Transport Association of Canada 2003, Usman et al. 2010).

A method to determine both real-time and near-future RSCs will allow respective transportation agencies to make more informed decisions that not only improve the safety of roads, but substantially cut down on WRM operational costs while maintaining a high level of service.

To help support and facilitate winter maintenance decisions, an advanced ITS monitoring technology known as road weather information systems (RWIS), available in both stationary and mobile stations, have been utilized by transportation agencies around the world. Through RWIS technologies, users are provided with real-time and forecasted weather and RSC information. Highway maintenance personnel use the information to improve the efficiency and effectiveness of their maintenance operations. The only downside is that installing and operating RWIS stations is costly and, because of this, most transportation agencies only deploy RWIS stations to a limited number of locations, hampering the coverage and effectiveness that they provide. As a result of the limited coverage issue, transportation agencies have been looking ways to infer road weather and surface conditions with the spatially limited RWIS information that they possess—so they can make the most out of their available resources and at the same time maximize their return on investment.

1.2 Road Weather Information Systems

In the mid-1980s, several US state departments of transportation (DOTs), including Minnesota's, New Jersey's, Pennsylvania's, Washington's, and Wisconsin's evaluated the effectiveness of various pavement data collection methods during the winter months. Among the various methods tested, the DOTs discovered that the RWIS were the most reliable. And thus, further research into its practical applications began, where it was discovered that, if state highway agencies would base their WRM operations on the weather and pavement condition information provided by RWIS, their operations would become more efficient and effective (Boselly 2001).

RWIS can be described as a combination of advanced technologies that collect, transmit, and disseminate road weather and surface condition information to data hubs, where it is then processed and made accessible to the general public. Road maintenance personnel have access to the data in near real-time and make use of it to effectively plan their WRM activities to shorten response times and reduce material usage (e.g., salt and sand). RWIS stations collect data using environmental sensor stations (ESSs) and live-broadcast cameras to provide real-time and forecasted roadway-related weather and surface conditions. Implementation of these systems not only enables cost-effective WRM but also helps motorists make more informed decisions for their travel. For this reason, RWIS have been widely used in many places in the northern hemisphere.

North America alone has more than 3,000 RWIS stations currently in operation and is continuing to expand their networks to improve their existing WRM services (Kwon et al. 2017, Kwon and Gu 2017). This section focuses on introducing the two general types of RWIS stations, stationary and mobile, along with discussions on their corresponding advantages and limitations.

Stationary RWIS stations, as depicted in © 2019 L. Gu, M. Wu, and T. J. Kwon, University of Alberta, Edmonton

Figure 1-1, are generally installed alongside the roadway, with the main purpose of closely monitoring weather/road surface conditions.



© 2019 L. Gu, M. Wu, and T. J. Kwon, University of Alberta, Edmonton

Figure 1-1. Typical stationary RWIS

Each station typically has the following components: cameras, road surface sensors, remote processing units (RPU), and communication hardware. In terms of the weather and road surface measurements collected, they will often include, but are not limited to, air temperature, road surface temperature, dew point, wind speed and direction, and surface status.

A mobile RWIS station, on the other hand, is installed on a vehicle, as shown in Figure 1-2.



© 2019 L. Gu, M. Wu, and T. J. Kwon, University of Alberta, Edmonton

Figure 1-2. Mobile RWIS unit equipped with spectral road surface temperature sensors

These mobile stations are equipped with a similar suite of sensors and dash cameras that allow the vehicles to collect weather and road surface data as they travel along the roadway. The data collected by a mobile RWIS unit is sent via cellular communication to the operations center. Apart from the measurements that are often collected by the stationary RWIS, some mobile RWIS units can also provide direct measurements of roadway treatment chemical concentration and pavement friction, which can help maintenance agency staff to utilize treatment methods that better match the actual weather/road surface conditions.

Due to different data collection mechanisms, stationary RWIS stations provide highly temporal but spatially limited coverage, while mobile RWIS units provide spatially continuous but temporally discrete measurements. Regardless of the differences, both systems are effective in collecting and disseminating weather and road condition information.

In terms of installation costs, a stationary RWIS station with basic functions costs more than \$50,000 (Canadian dollars) to install, and this does not include continuous maintenance costs and additional sensors that one might want (Buchanan and Gwartz 2005). Considering the relatively high price tag, finding the optimal locations for RWIS stations has always been a challenge to highway planning authorities, as it is not economically feasible to have a RWIS network with high spatial density. Additionally, the reliability of point measurements collected diminishes as the distance between RWIS stations increases, resulting in an incomplete map of surface conditions.

One possible solution could be utilizing information obtained from mobile RWIS units to fill in the gaps between stationary RWIS locations, improving the RWIS and extending its spatial representation. For example, thermal mapping (TM) is one of the earlier techniques that aims to construct the spatial distribution of road surface temperature profiles over a highway.

In previous thermal mapping-related studies, a vehicle equipped with a mounted infrared thermometer collected data under different weather conditions, which were then graphically depicted by drawing thermal maps or fingerprints (Shao et al. 1996, Chapman et al. 2001a and 2001b, Marchetti et al. 2011). In other similar studies, areas that are likely to be freezing or snow covered are shown to be visually identifiable through the use of thermal maps. This technique allowed maintenance personnel to quickly identify hotspots, but it required frequent monitoring (Marchetti et al. 2014).

Unfortunately, due to limited budget and manpower, it is an unrealistic expectation to continuously collect high quality and spatially continuous information in frequent intervals. Nevertheless, given large spatial areas and long temporal periods that need to be monitored, it is important to understand how RSCs vary over distances and time to help maintain safe driving conditions and reduce the costs of WRM activities. To resolve this deficiency, focus must move away from just measuring and toward modeling using rich data sources collected via intelligent road weather sensors.

1.3 Current Practice of Winter Road Surface Conditions Estimations

Several numerical models have previously been proposed in an attempt to quantify the spatial distribution of RSCs. Sass (1992) developed a prediction model based on heat condition and the surface energy-balance models. Chapman et al. (2001a and 2001b) proposed a multiple regression model to demonstrate that up to 75% of the residual RST variation can be affected by surrounding geographical features using thermal mapping techniques. Sokol et al. (2017) applied an ensemble technique for RST forecasting using an energy balance and heat conduction model where the results tended to underestimate the true values.

Perchanok (2002) conducted a discriminant analysis using three friction measurements: peak resistance (F_p), slip speed at which the peak resistance occurs (V_{crit}), and locked wheel resistance (F_{60}). These three measurements were used to classify RSCs into categories such as bare wet, bare dry, loose snow, packed snow, and slush. The analysis built a series of linear discriminant functions that could optimally discriminate different RSC types.

Although these prior studies helped provide some insights into how RSCs vary, they suffered from one major limitation: the models were developed to provide only site-specific RSC information rather than for an entire segment of road. Having continuous RSC information over a road network is critical, not only to road users for improved safety but also to winter maintenance personnel who are responsible for maintaining a good level of service.

Moreover, RSC estimation can be challenging as an ongoing adverse weather event can abruptly change within a short distance and is constantly influenced by many external factors including geographical, topographical, and meteorological features. Likewise, considering the high degree of uncertainty and randomness associated with inclement weather events and their interactions with complex road networks, it has become extremely difficult to accurately estimate conditions between RWIS stations.

1.4 Research Objectives

The main objective of this project was to develop a systematic and transferable method for estimating RSCs using data from both stationary and mobile RWIS stations and two advanced modeling techniques: regression kriging (RK) and deep learning (DL). The research had four specific objectives as follows:

- Develop a spatially continuous method of mapping the characterization and spatial variations of road weather and surface conditions
- Prepare and process event-based RWIS and other data sets (e.g., weather, traffic, camera images, remotely sensed digital elevation models) that are required for both spatial mapping and image recognition
- Test and/or improve the existing image recognition models using the new training/testing data
- Implement a web-based application for showcasing the developed spatial mapping solution and demonstrate the application with real-world usage scenarios

The project study area was a stretch of interstate highway located in Iowa. Along this stretch, stationary RWIS stations, imagery, and other remote sensing and geographic information system (GIS) data sets were collected. These collected data sets were then processed and linked by time and space, and then utilized to determine the two key variables of interest in this study: road surface temperature (RST) and road surface index (RSI).

RST was selected for investigation as it is required to generate accurate road weather forecasts as well as to predict black-ice potential. RSI was selected because it is considered one of the most important performance indicators given it measures the effects of various winter maintenance operations on road users (i.e., level of service).

This report is organized as follows: Chapter 2 describes the proposed methodology for estimating RSCs using the stationary and mobile RWIS. Chapter 3 is a discussion on the study area and the data sets collected. Chapter 4 focuses on the results of a real-world case study to demonstrate its real-world applications. Finally, the last chapter, Chapter 5, summarizes the main findings of this project and presents possible future research extensions that can build on the work done thus far.

2. METHODOLOGY

RSC estimation has been the topic of study for researchers, road maintenance authorities, and policy makers for many years. However, obtaining accurate estimations are difficult due to the inherent variability of road weather and surface conditions, especially during inclement weather events. To help tackle this challenge, the researchers explored and evaluated two advanced RSC modeling techniques, RK and DL, .

RK is a geostatistical interpolation method that has garnered a lot of attention recently, as it has the capability to estimate RSCs between existing RWIS stations with the help of covariates that are known to affect the spatial variation along a highway segment. The novelty of this method lies in the utilization of point measurements from RWIS stations to quantify the underlying spatial structures via a semivariogram model.

Another method adopted for RSC estimations is DL due to its potential to recognize and classify RSC images into descriptive measures (such as snow coverage level). As previously mentioned, the two key variables of interest in this study were RST and RSI (converted from RSC). RST is indispensable for predicting black-ice potential and for the efficient mobilization of WRM services, while RSI is a friction-like surrogate measure used to quantify the level of service.

The data (i.e., RST and RSI) for developing and evaluating the proposed RK method can be obtained from multiple sources. Mobile RWIS units, as mentioned previously, provide the continuous measurements with location attributes (e.g., longitude and latitude) of each RSC data point including those for RST and RSC images, which allows the investigation of spatial variation patterns and exploration of weather event characterization. To obtain the RSI values, RSC images are used to develop DL models and, by feeding in new images, the predicted RSC categories by DL are converted into RSI values accordingly.

Other auxiliary information, such as meteorological factors and topographical features are also needed as input to the RK method. Data from stationary RWIS stations provide point measurements, which can be used as reference data to evaluate the feasibility and reliability of the proposed method for RST and RSI estimation. The overall workflow for this methodology is illustrated in Figure 2-1.

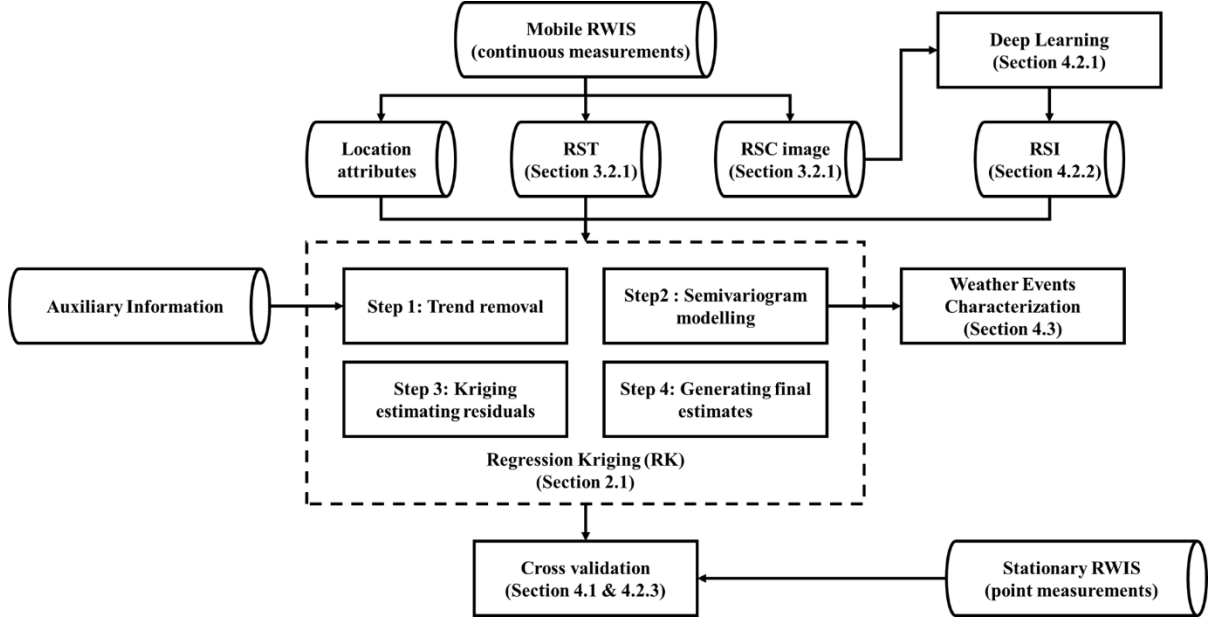


Figure 2-1. Workflow of the proposed framework

Each process is further explained in later sections, followed by a case study demonstrating the practical use case for this framework.

2.1 Regression Kriging

2.1.1 The Idea

Kriging has an extensive history that saw its beginnings in the mining industry. It was originally conceived by D. G. Krige and later formally defined mathematically by G. Matheron establishing the field of linear geostatistics called Kriging (Krige 1981, Cressie 1990). Kriging is able to predict values at unvisited/unmeasured sites by using a stochastic model to measure the continuous spatial variation of sparse sample points. It differs from traditional mathematical interpolation methods, as kriging takes both the deterministic and stochastic components of random variables into consideration. Not only does it provide point estimates, but it also gives the uncertainty of its estimates at the unknown locations based on the set of known observations, as follows.

Let x be location vectors for the estimation point and x_k be a set of observations at known locations, with $k = 1, \dots, n$, and Z be a random variable of interest (i.e., RSC in this study). The expression of a general kriging model is as follows (Goovaerts 1997):

$$\hat{Z}(x) = m(x) + \sum_{k=1}^m \lambda_k [Z(x_k) - m(x_k)] \quad (1)$$

where $\hat{Z}(x)$ is the estimated value of the target variable at a location of interest. The terms $m(x)$ and $m(x_k)$ are the expected values (means) of the random variables $Z(x)$ and $Z(x_k)$ and λ_k is a

kriging weight determined by the spatial dependence structure of the residual. With the kriging weights known, it allows the user to determine the kriging estimation variance by equation (2):

$$\sigma^2(x_0) = \begin{bmatrix} \lambda_1 \\ \lambda_2 \\ \vdots \\ \lambda_k \\ \mu \end{bmatrix}^T \begin{bmatrix} \gamma(x_0, x_1) \\ \gamma(x_0, x_2) \\ \vdots \\ \gamma(x_0, x_k) \\ 1 \end{bmatrix} \quad (2)$$

where $\sigma^2(x_0)$ is the kriging estimation variance for location x_0 , λ is the kriging weights that can be found later in equation (5), and μ is the Lagrange parameter involved in the kriging weights calculation.

Over time, many variations of kriging have been developed based on different assumptions for $m(x)$ (i.e., the deterministic component). For example, simple kriging (SK) assumes a known global mean while ordinary kriging (OK) assumes an unknown global mean (Cressie 1990, Oliver and Webster 1990). In recent years, an interest in hybrid interpolation techniques has arisen, to incorporate two conceptually different methods to model and map spatial variability and strengthen the explanation of the target variable.

One of the most renowned hybrid interpolation methods is RK, which makes estimations by first using regression on auxiliary information (e.g., meteorological factors, geographical features) for the deterministic component and then using OK to interpolate the stochastic component (i.e., residuals). The final estimate for one location is the summation of these two estimated components (Hengl et al. 2007, Ligas and Kulczycki, 2010, Odeh et al. 1995, Hengl et al. 2003). RK equations are shown in equations (3) through (5):

$$\hat{Z}(x) = \hat{m}(x) + \hat{e}(x) = \sum_{i=0}^p \hat{\beta}_k \cdot q_k(x) + \sum_{k=1}^m \lambda_k \cdot e(x_k) \quad (3)$$

where $\hat{m}(x)$ is the fitted deterministic part, $\hat{e}(x)$ is the interpolated residual, $\hat{\beta}_k$ are coefficients of the estimated drift model, $\hat{\beta}_0$ is the estimated intercept, p is the number of auxiliary variables, λ_k are kriging weights, and $e(x_k)$ is the regression residual. The regression coefficients $\hat{\beta}_k$ can be determined by any appropriate fitting method, e.g., ordinary least squares (OLS) or, optimally, using generalized least squares (GLS) to take the spatial correlation between individual observations into account (Cressie 2015). Equation (4) and (5) show how $\hat{\beta}_k$ are obtained by using GLS and λ_k by using OK, respectively.

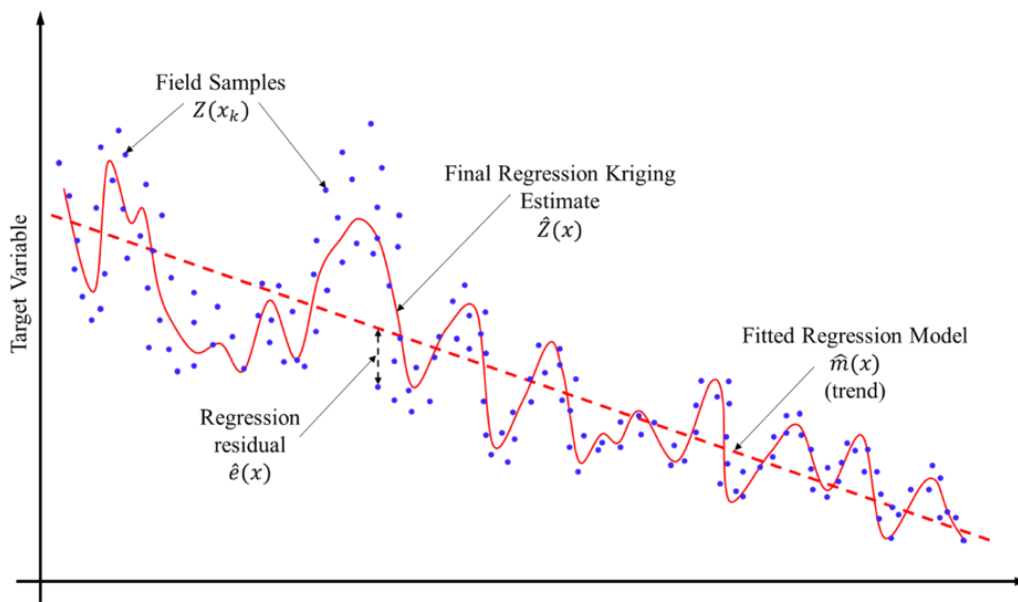
$$\hat{\beta}_{GLS} = (q^T \cdot C^{-1} \cdot q)^{-1} \cdot q^T \cdot C^{-1} \cdot z \quad (4)$$

where $\hat{\beta}_{GLS}$ is the vector of estimated regression coefficients $\hat{\beta}_k$, C is the covariance matrix of the residuals, q is a matrix of predictors at the sampling locations, and z is the vector of measured values of the target variable.

$$\begin{bmatrix} \lambda_1 \\ \lambda_2 \\ \vdots \\ \lambda_k \\ \mu \end{bmatrix} = \begin{bmatrix} \gamma(x_1, x_1) & \cdots & \gamma(x_k, x_1) & 1 \\ \vdots & \ddots & \vdots & \\ \gamma(x_1, x_k) & \cdots & \gamma(x_k, x_k) & 1 \\ 1 & \cdots & 1 & 0 \end{bmatrix}^{-1} \begin{bmatrix} \gamma(x_0, x_1) \\ \vdots \\ \gamma(x_0, x_k) \\ 1 \end{bmatrix} \quad (5)$$

where γ is the semivariance between two locations and its equation can be found subsequent to this discussion in equation (6).

Figure 2-2, adapted from Gu et al. (2019), provides a schematic example of the general concepts of RK.



Adapted from Gu et al. 2019, © 2019 L. Gu, M. Wu, and T. J. Kwon, University of Alberta, Edmonton

Figure 2-2. Example of a regression kriging process

As can be seen from this figure, the deterministic part of the variation is first estimated using a multiple linear regression (MLR) model to remove the possible trend, and then the residuals can be interpolated by kriging, which characterizes and quantifies the underlying spatial structure of the observed measurements. The estimated residuals are then added back to the regression results to generate the final estimations.

2.1.2 Quantifying Spatial Structures via Semivariogram

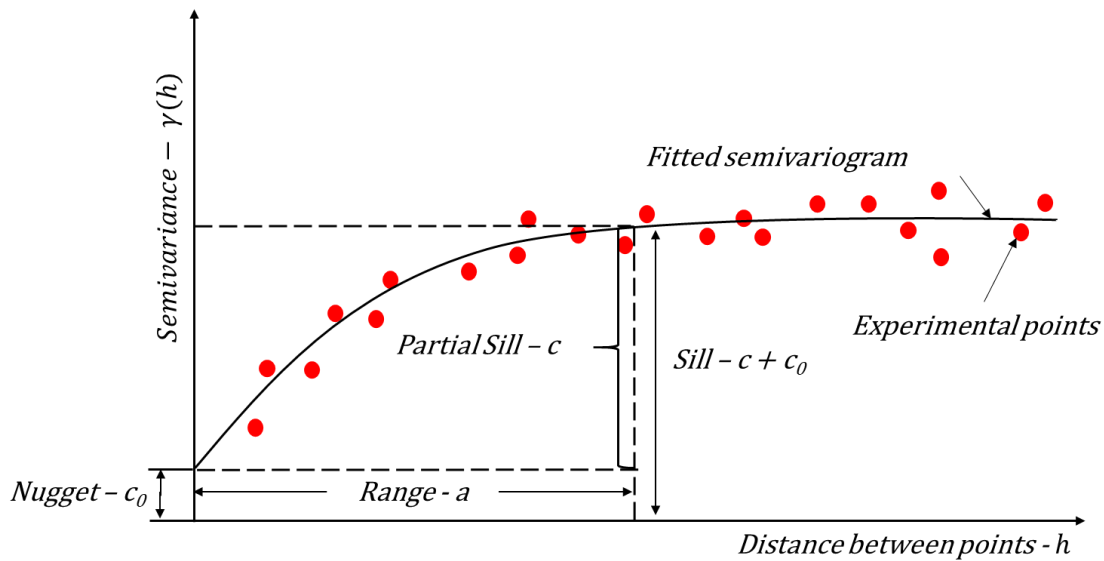
Like all other geostatistical models, the fundamental assumption underlying RK is that the observations are spatially autocorrelated and the underlying correlation structure can be represented by a semivariogram. A semivariogram model depicts how the data are correlated with themselves as a function of the spatial distance based on observations and location information (Journel and Huijbregts 1978). In reality, the data points are quite scarce, and,

because of this, the data points are typically grouped per distance vector, h , and the semivariogram model is calculated as half the variance of this difference (Curran 1988). Equation (6) is used to calculate the sample semivariance for a separation distance, h .

$$\hat{\gamma}(h) = \frac{1}{2m(h)} \sum_{k=1}^{m(h)} [Z(x_k) - Z(x_k + h)]^2 \quad (6)$$

where $\hat{\gamma}(h)$ is the sample semivariance, $Z(x_k)$ is a measurement taken at location x_k , and $m(h)$ is the number of observations pairs separated by the lag, h , in the direction of the vector.

The three key parameters used to describe a semivariogram model are called the nugget, sill, and range. These three parameters are illustrated in Figure 2-3 (Curran 1988).



Adapted from Gu et al. 2019, © 2019 L. Gu, M. Wu, and T. J. Kwon, University of Alberta, Edmonton

Figure 2-3. A semivariogram and its associated parameters

The nugget represents microscale variations, measurement errors, or any spatial variability that exists at a distance smaller than the shortest distance between two measurements. The range indicates the separation distance limit where the data points are considered autocorrelated to each other (i.e., values separated by distances greater than this are considered uncorrelated). The upper bound is known as the sill and represents the variance of the random field (Curran 1988).

Since it is customary to use more than 50 samples to build a reliable semivariogram model (Olea 2006), sufficient RSC data collected by mobile RWIS units are used to construct semivariograms as priori information to estimate the RSC along roadways. Several multiple theoretical formulas can be used to fit an experimental semivariogram, Table 2-1 shows the expressions for some commonly used theoretical semivariogram models (Armstrong 1998, Bohling 2005).

Table 2-1. Commonly used theoretical semivariogram models

Model	Expression
Spherical	$\gamma(h) = \begin{cases} 0 & , h = 0 \\ c_0 + (c - c_0) \left(1.5 \left(\frac{h}{a} \right) - 0.5 \left(\frac{h}{a} \right)^3 \right) & , 0 < h < a \\ c & , h \geq a \end{cases}$
Exponential	$\gamma(h) = \begin{cases} 0 & , h = 0 \\ c_0 + (c - c_0) \left(1 - e^{-\frac{3h}{a}} \right) & , h > 0 \end{cases}$
Gaussian	$\gamma(h) = \begin{cases} 0 & , h = 0 \\ c_0 + (c - c_0) \left(1 - e^{-\frac{(3h)^2}{a^2}} \right) & , h > 0 \end{cases}$
Linear	$\gamma(h) = \begin{cases} 0 & , h = 0 \\ h & , h > 0 \end{cases}$
Cubic	$\gamma(h) = \begin{cases} 0 & , h = 0 \\ c_0 + (c - c_0) \left(7 \left(\frac{h}{a} \right)^2 - 8.75 \left(\frac{h}{a} \right)^3 + 3.5 \left(\frac{h}{a} \right)^5 - 0.75 \left(\frac{h}{a} \right)^7 \right) & , 0 < h < a \\ c & , h \geq a \end{cases}$
Cardinal sine	$\gamma(h) = \begin{cases} 0 & , h = 0 \\ c_0 + (c - c_0) \left(1 - \frac{\sin \left(\frac{h}{a} \right)}{\left \frac{h}{a} \right } \right) & , h > 0 \end{cases}$

where: γ is the semivariance, h is the points separation distance, c_0 is the nugget, a is the range, and c is the sill

2.1.3 Implementation and Evaluation

The following steps are needed to build a semivariogram model from mobile RWIS observations, as well as to combine them with RK to interpolate RSC.

Step 1: Remove trends for RSC. This step involves developing a model for two purposes: determine the covariates (e.g., latitude and elevation) and detrend the RSC data. The RSC data are detrended because mobile RWIS units provide continuous measurements in the construction of the spatial autocorrelation structure.

Step 2: Construct semivariogram models using detrended RSC obtained from Step 1. With detrended RSC (i.e., residuals) obtained from Step 1, the semivariogram models are constructed and calibrated using the residuals as the experimental points. A fitted semivariogram model is then chosen to represent the spatial structure that will be used in the subsequent steps.

Step 3: Perform kriging to generate estimated residuals from the measured residuals obtained in Step 1. In this step, kriging is utilized to generate estimated residuals based on the residuals that were calculated from Step 1; semivariogram models calibrated in Step 2 are used here as priori information.

Step 4: Generate final RSC estimates. This step generates the final RSC estimates by adding the estimated residual results in Step 3 back into the linear regression predicted results from Step 1.

To evaluate the estimation accuracy as well as its feasibility, cross validation is done to compare the RK estimates with the actual observed RSC values collected by the mobile RWIS unit. Cross validation is a resampling procedure used to evaluate the developed model on a limited data sample set. In a leave-one-out cross validation method, it is typically done iteratively for all data locations by removing a data point from each location, and then making an estimate at the removed point using the developed model and the surrounding data points.

In our case, only point measurements from the locations of existing RWIS stations were used as inputs, along with the pre-constructed semivariogram models that were used to estimate RSC at an unmeasured location. Following this, the prediction and the observed value were compared to evaluate the feasibility of RK.

To better evaluate model performance, the root mean square error (RMSE) is typically used to validate the goodness-of-fit between estimated and observed RSC. RMSE indicates how closely the model estimates the measured values. Equation (7) is for the RMSE.

$$RMSE = \sqrt{\frac{\sum_{i=1}^n (x_i - \hat{x}_i)^2}{n}} \quad (7)$$

where n is the total number of observations and x_i and \hat{x}_i are the observed RSC and RK estimated RSC in site i , respectively.

Other than the RMSE, other statistical measurements, including mean absolute error (MAE), average standard error (ASE), and root mean square standardized error (RMSSE) are also often adopted. These alternative statistical measurements are used to quantitatively assess the goodness of fit of the developed model from other aspects (e.g., standard error compares sample mean and population mean); in this report, only RMSE is included.

2.1.4 Weather Events Characterization via Nugget-to-Sill Ratio

Another task of this project was to generalize the characterization of weather events via RSC spatial variation pattern, which can be achieved by examining the potential relationship between hourly RSC spatial dependence and the corresponding weather events (e.g., wind and rainfall) that happened within the same specific hour. Spatial dependence refers to the degree of spatial autocorrelation between independently measured values observed in geographical space and is necessary for the determination of kriging weights (Cambardella et al. 1994).

With the semivariogram model calibrated, the nugget-to-sill ratio (NSR), which is calculated by dividing the nugget by the sill, can be utilized as a dimensionless measure of the proportion of total observed variation that could not be explained by the observed spatial dependence of the target variable (Cambardella et al. 1994, Sun et al. 2019). In other words, a small NSR represents a strong spatial dependence, while a large ratio reflects a weak spatial dependence on the variable. For example, the randomly distributed RST tends to have a large NSR value as the variations in different lag distances fluctuate and thus do not fit any pattern.

According to the literature (Cambardella et al. 1994, Sun et al. 2019, Karl and Maurer 2010, Behrens et al. 2019), three distinct classes of spatial dependence are typically defined in accordance to NSR values as follows: if the ratio is smaller than 25%, the target variable is considered strongly spatially dependent; if the ratio is between 25% and 75%, the variable is considered moderately spatially dependent; and if the ratio is greater than 75%, the variable is considered weakly spatially dependent. Sample semivariograms of the three classes are shown in Figure 2-4.

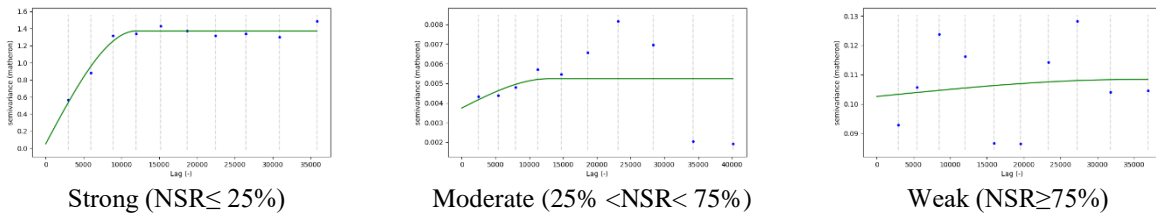


Figure 2-4. Sample semivariograms of different spatial dependence classes

2.2 Deep Learning

2.2.1 The Idea

Although RK is effective in estimating values at unmonitored areas, its value to WRM authorities is greatest when real-time point measurements of RSC are obtained in a timely manner, so that it can be used as input in the RK technique quickly. Traditionally, RSC monitoring is done by manual patrols by highway agencies or maintenance contractors or by using RWIS stations, with each having their own limitations.

Manual observation by patrollers is typically subjective, inaccurate, and time-consuming, particularly since the patrollers will often need to monitor a large area. Some new technologies, such as in-vehicle video recorders, smartphone-based systems, and high-end imaging systems have been developed to collect RSC data; however, the application of these technologies still requires manual image processing as no readily available and reliable computerized image recognition solutions are available to automate this process (Pan et al. 2020). Researchers have also attempted to apply some traditional machine learning models, including artificial neural networks (ANNs), random forests (RFs), and support vector machines (SVMs) to classify winter RSC images; however, these models have shown poor accuracy and transferability to date (Pan et al. 2020, Carrillo et al. 2019). This is changing with the development of a novel machine learning technique –DL or deep neural networks (DNNs).

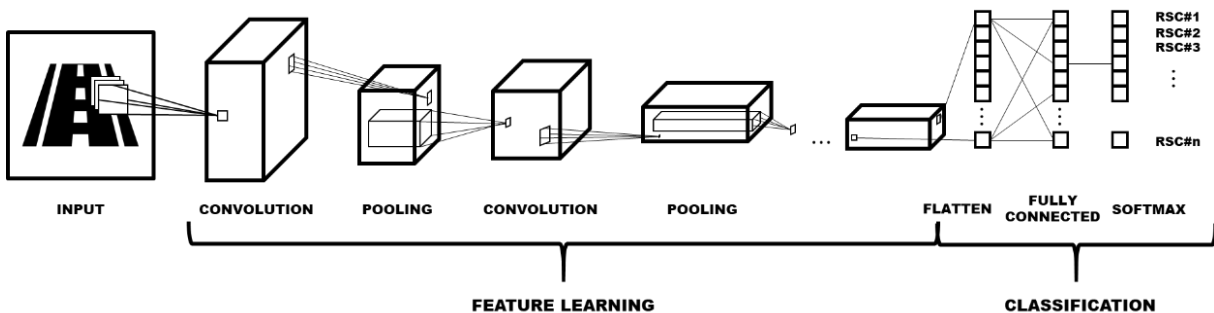
DL models have been extensively studied and shown excellent performance to solve a variety of problems including unsupervised learning-based classification, object detection, forecasting, etc. Previous studies have also shown some promising results when applying DL for tackling RSC recognition problems (Pan et al. 2020, Carrillo et al. 2019, Pan et al. 2019).

2.2.2 Implementation and Evaluation

In this subsection, the implementation of the DL model is elaborated on, along with a description of the model architecture, as well as a demonstration of its usage in RSC image recognition.

DL models are an evolution of a simpler type of model called the multi-layer perceptron (LeCun et al. 2015), which takes an input vector and uses consecutive groups of non-linear functions, called layers, to produce higher-level representations of the input data. In contrast, DL models use many layers, where each succeeding layer takes the output of the previous layer as its input. Most DL models fall into the category of supervised learning because their goal is to make the model create a desired output mapping from input observations. In our particular case, we expect the DL models to receive images from in-vehicle cameras paired with mobile RWIS units.

Figure 2-5 shows a simplified architectural diagram of DL models for image classification.



Adapted from Carillo et al. 2019 who cited mathworks.com and that original has Creative Commons Attribution 4.0 International Free Cultural Works license and approval

Figure 2-5. Generic architecture of a DL model for image classification

An input image is represented by a three-dimensional matrix with the height, width, and red-green-blue (RGB) channels of the image as its initial dimensions. This input image moves through the layers in the model and, by the end of it, the model outputs a vector of probabilities with the highest probability corresponding to the most likely RSC category for the image.

The first component (feature learning) of a DL model includes a series of convolutional and pooling layers that gradually convert the information contained in the input image into a compressed vector representation with smaller height and width but a larger number of channels than the original image. Convolutional layers are also known as filters that summarize an input matrix into one with smaller dimensions. In other words, these layers learn how to detect features such as shapes, contrast patterns, and color variations, and pass along a simplified representation of these features to the following layers.

The second component (classification) starts with a layer that converts the three-dimensional vector from the first section into a one-dimensional vector (flattening), which is then fed into a series fully connected layers that reduce the size of the vector representation even more, and

then, finally, through a softmax layer (Jang et al. 2016, Wang et al. 2018) that outputs probability values for each category in the classification task. Fully connected layers are usually implemented in the last part of the model to summarize the visual features detected by the previous layers. Most DL models have many convolutional layers but only a few fully connected layers because the number of parameters in the latter ones is much higher, which in turn requires more computational resources to train the models.

The design of a DL model also includes the consideration of multiple hyperparameters, and their role is crucial for the successful implementation of the model. The designer can set hyperparameters to manage multiple aspects of the model, but to fine tune them requires significant effort and application domain knowledge. By setting these parameters, the designer can define the number of neurons per layer, the type of non-linear functions (i.e., activation functions) to use, the number of times the data set is passed through the model during training (i.e., epochs), how fast the model learns (i.e., learning rate), and the dropout regularization rate (Dahl et al. 2013, Gal and Ghahramani 2016), among other characteristics of the model definition and training. In practice, researchers focus on fine-tuning the most relevant hyperparameters based on previous literature and their experimental findings.

A DL model is typically trained using 90% of all labeled RSC images and then validated using the remaining 10% (Khan et al. 2019, Hamori et al. 2018). When training accuracy is very low, it is called an “underfitting” problem, which means the DL model is not capable enough to learn useful features from the images. In contrast, when training accuracy is high but validation accuracy is very low, this is called an “overfitting” problem, meaning the DL model cannot well generalize the pattern learned from the training data sets. In our case, both problems were taken into account during development of the DL model.

3. STUDY AREA AND DATA

To evaluate the feasibility of RK and DL for estimating RSCs along highways as well as the NSR for characterizing weather events, the content of this chapter demonstrates a real-world case study example. The descriptions and results associated with each part of the study are presented following the considerations outlined in the study area section .

3.1 Study Area

Since RSC can easily be influenced by a variety of factors, the selection of the study area must consider and control for any geographical, topographical, and traffic related effects. In addition, considering the fact that harsh weather events affect a long stretch of roadway and that winter maintenance activities can be done at the same time along a highway, the spatial coverage needs to be considered during the study area selection process. Therefore, a road section that was completely paved with asphalt in the southern section of I-35 within Iowa was selected for this study. The study area is shown in Figure 3-1.

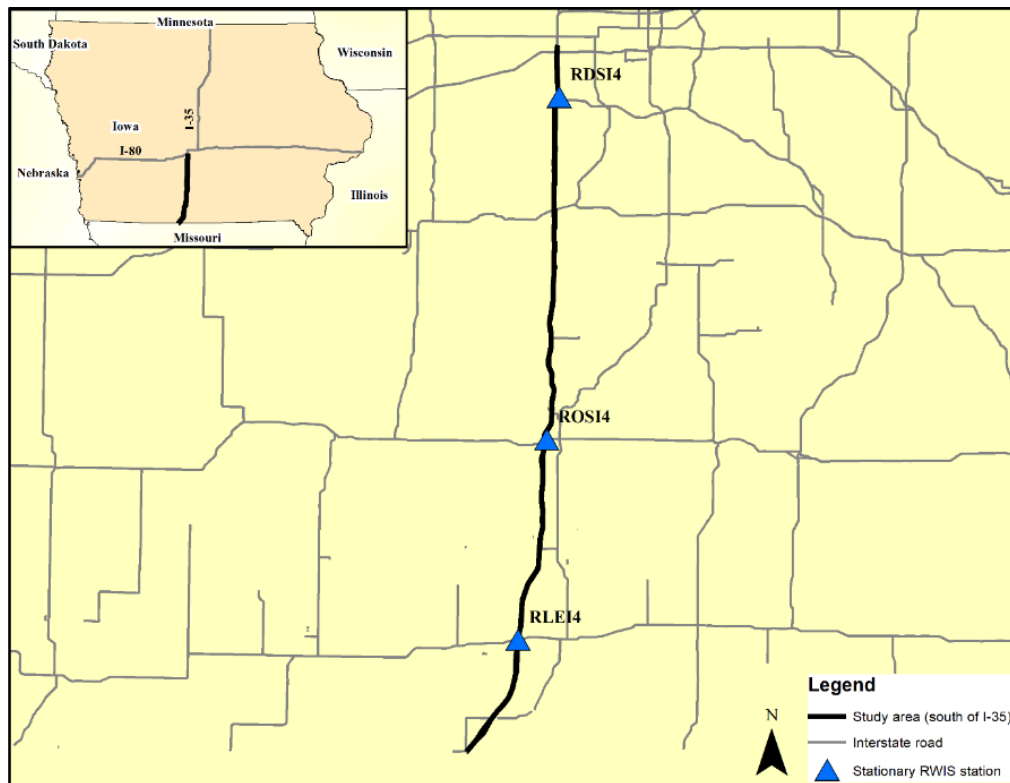


Figure 3-1. Study area - southern section of I-35 in Iowa

The selected road segment goes through four counties in Iowa and overlaps with I-80 in central Iowa. Due to its importance to both the US and Iowa, the Iowa DOT spends a lot of resources to monitor and improve conditions on this road segment. The total length of this stretch is about 73.32 mi (118 km), with three stationary RWIS stations located within its range.

RST data and RSC images were collected by the automated vehicle location (AVL) system, which can be considered a stand-in version of a heavily simplified mobile RWIS unit, while other data (meteorological factors, geographical and topographical features, etc.) can be obtained using other data sources, including the three stationary RWIS stations. Details of these other data sources are described in the next section.

3.2 Data Description and Integration

3.2.1 Road Surface Temperatures and Dash Camera Images

RST and RSC images of the Iowa road network between October 2018 and April 2019 were collected by the AVL system, which is equipped with global positioning system (GPS) data to track the locations of the winter maintenance vehicle fleet, along with a regular thermometer and an inferred thermometer to measure the air temperatures and RST every 10 seconds along the roadway. A standard vehicle-mounted dash camera is utilized to record RSC images along the roadway every 5 to 10 minutes. Within the study area for the timeframe, 579,088 RST records and 24,586 RSC images were collected.

The RSC images were manually labeled according to the classification scheme shown in Table 3-1 through a web-based labeling platform, as shown in Figure 3-2.

Table 3-1. Definition of different RSC categories

Sample Images	RSC Description/Definition	RSC Category
	At least 9.84 ft (3 m) of the pavement cross-section in all lanes clear of snow or ice	Bare Pavement
	Only part of wheel path is clear of snow or ice	Partially Snow Covered
	No wheel path clear of snow or ice	Fully Snow Covered
	Not recognizable because images are too blurry, too dark, or too light	Undefined



Figure 3-2. Web-based manual image classifier

Labeled images were then used to train the DL model and validate its accuracy. Since RSI values were not directly collected by the AVL, RSC categories were converted into RSI values accordingly before they were implemented in the spatial mapping of the RSI for unvisited areas. The conversion method can be found later in section 0. on RSC categories (labeled RSC images), which was used in model development, with summary statistics for the images shown in Figure 3-3.

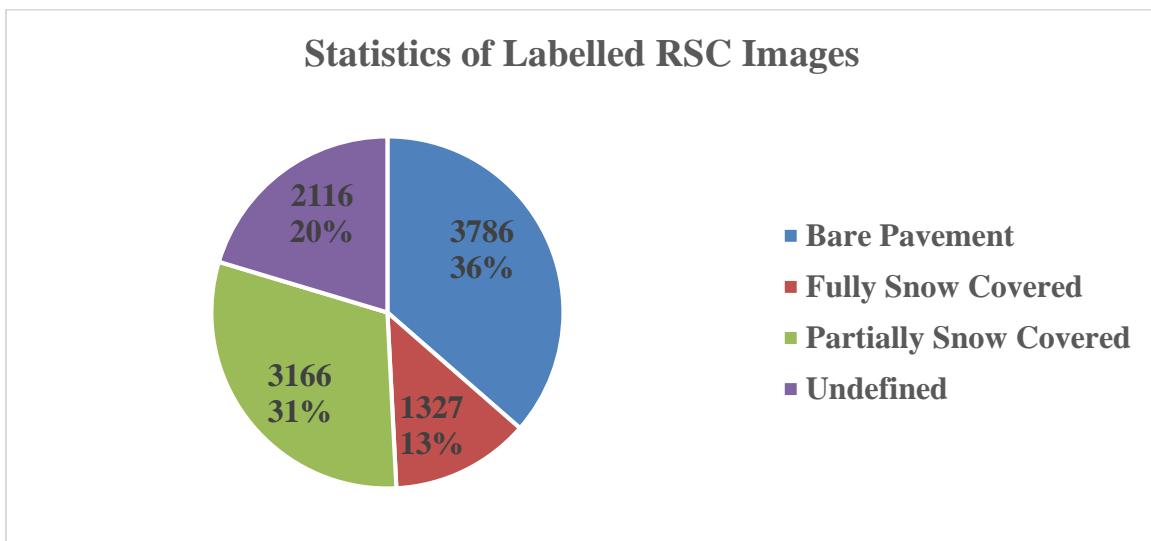


Figure 3-3. Statistics of labeled RSC images

To eliminate measurement errors and local random fluctuations of RST and RSI, raw data points were aggregated both spatially (every 546.8 yds [500 m]) and temporarily (ever hour) along the

road segment. In addition, to ensure each hourly period had enough observations to provide sufficient spatial coverage, only those with coverages longer than 40.4 m (65 km) (over half of the total stretch length) and more than 50 aggregated data points were kept for modelling (Olea, 2006). The descriptive statistics of the hourly RST and converted RSI values along the study area are shown in Table 3-2.

Table 3-2. Descriptive statistics of hourly AVL observation

Variable	#Hourly Observations	Minimum	Maximum	Mean.	Standard Deviation
RST	228	-13.1°C	28.3°C	-1.2°C	3.4°C
RSI	34	0.35	0.90	0.59	0.19

3.2.2 Digital Elevation Model

To obtain topographical features of the Iowa road network that included the study area, a digital elevation model (DEM) with a resolution of 128 gigabytes (GB) (for 3 m of data) was downloaded from the State of Iowa Open Geospatial Data website (at <https://geodata.iowa.gov/>) using a python web crawler script. The elevation, slope and aspect along the study area were then extracted from the DEM using ArcGIS 10.7 (ESRI 2011). The resulting map files for all topographical features had a size of 484 GB. Figure 3-4 shows an example the DEM.

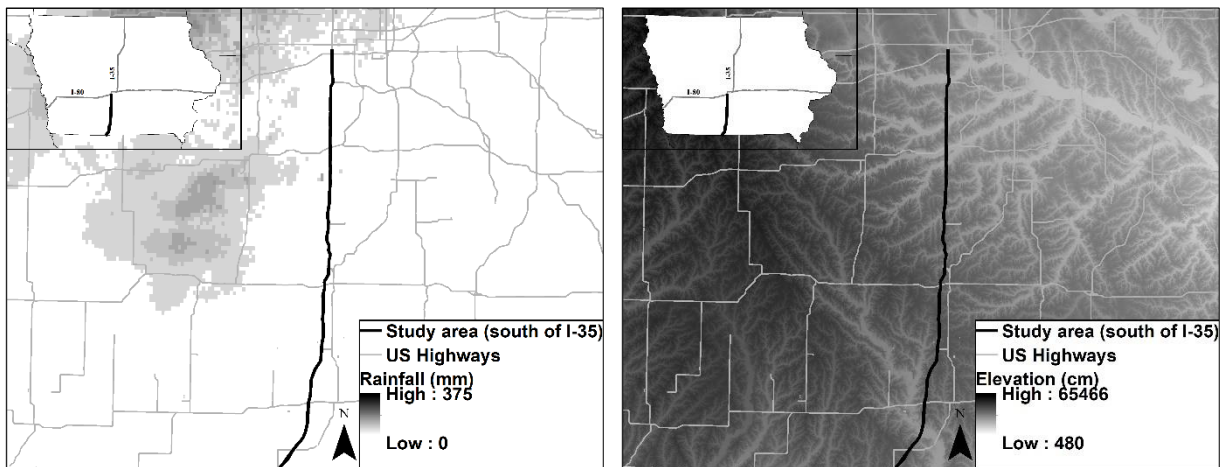


Figure 3-4. Data preparation. example of rainfall intensity (left) with elevations (right)

3.2.3 Meteorological Data

Meteorological data including but not limited to air/surface temperature, wind speed/direction/gust, and rainfall for the entire state between October 2018 and April 2019 (seven months of data) were downloaded from the Iowa State University Iowa Environmental Mesonet (IEM) Roadway Weather Information site (at <http://mesonet.agron.iastate.edu/RWIS/>). Some of the data (e.g., wind relation factors) were in comma-separated values(CSV) files and

collected by RWIS stations at 15- to 20-minute intervals, while other data (e.g., rainfall) were in raster image format and collected by remote sensors. The total size of the downloaded files was about 7.5 GB. In the end, the data collected by the three RWIS stations in the study area were processed and integrated for the following analysis.

An example of the meteorological data (e.g., rainfall) is shown in the previous Figure 3-4. The temporally continuous meteorological factors were used to examine the correlation between RSC's spatial dependence and the meteorological factors themselves. Wind-related factors and rainfall intensity were used to characterize the weather events.

It is important to note that the study area is a stretch of roadway running in the north-south direction. A re-Calculated directional Wind Speed (CWS) that integrates wind speed (WS) and wind direction (WD) based on the degrees from the north-south direction was calculated for each wind record via vector calculation rules; the directional effects of wind on RSC variations can thus also be controlled. All meteorological factors were aggregated hourly, and the descriptive statistics for the hourly wind factors and rainfall are shown in Table 3-3.

Table 3-3. Descriptive statistics of hourly meteorological factors

Factor	Month	Mean	Max.	Min.	Std.
WS (m/s)	Oct.	0.94	0.94	0.94	0.00
	Nov.	5.59	9.06	1.00	2.32
	Dec.	3.64	6.22	1.50	1.60
	Jan.	3.67	7.39	0.92	1.58
	Feb.	2.67	6.39	1.40	1.74
	Mar.	4.25	4.29	4.17	0.07
	Apr.	3.04	3.04	3.04	0.00
WD (°)	Oct.	69.45	69.45	69.45	0.00
	Nov.	22.05	63.25	7.55	11.97
	Dec.	48.48	79.87	17.47	17.38
	Jan.	38.86	84.82	9.46	20.87
	Feb.	33.52	44.14	22.07	8.59
	Mar.	67.63	68.97	64.96	2.32
	Apr.	31.67	31.67	31.67	0.00
CWS (m/s)	Oct.	0.26	0.26	0.26	0.00
	Nov.	5.09	8.80	0.38	2.27
	Dec.	1.96	4.03	0.41	1.10
	Jan.	2.68	7.26	0.26	1.94
	Feb.	1.94	4.45	1.00	1.15
	Mar.	1.21	1.28	1.18	0.05
	Apr.	2.34	2.34	2.34	0.00

Factor	Month	Mean	Max.	Min.	Std.
WG (m/s)	Oct.	2.11	2.11	2.11	0.00
	Nov.	8.89	14.13	1.87	3.68
	Dec.	5.81	9.97	2.56	2.50
	Jan.	5.79	11.12	1.71	2.42
	Feb.	4.30	10.61	2.49	2.65
	Mar.	6.44	6.44	6.44	0.00
	Apr.	5.48	5.48	5.48	0.00
Rainfall (mm)	Oct.	0.00	0.00	0.00	0.00
	Nov.	4.60	25.00	0.00	6.16
	Dec.	1.88	25.00	0.00	5.56
	Jan.	3.86	20.00	0.00	4.69
	Feb.	0.00	0.00	0.00	0.00
	Mar.	3.00	5.00	2.00	1.41
	Apr.	0.00	0.00	0.00	0.00

m/s = meters per second, mm = millimeters, Max. = maximum; Min. = minimum; Std. = standard deviation

4. RESULTS AND DISCUSSION

4.1 Spatial Mapping of Road Surface Temperatures

Following the previously described procedures, the RK model can be developed via a few key steps. First, trend removal is performed to see how much variance in the RST can be explained by air temperature and the selected geographical features of latitude, longitude, altitude, and slope. Secondly, a semivariogram model is applied to quantify the spatial variation of the detrended RST. Following this, the kriging interpolation approach is used to modify the estimated RST obtained from the first step. The last part of the process is the cross validation of the final estimated results.

In this section, four examples are selected to illustrate the overall procedure and its associated results, while the complete results including all hourly events are included in Appendix A.

The trend removal was performed by fitting an MLR model using GLS to ensure the target variable (i.e., RST) was free of trend. A *p*-test was then done to confirm the statistical significance between RST, air temperature, and each geographical feature at a 5% significance level. Table 4-1 shows the fitted trend model results of the selected four examples in the study area.

Table 4-1. Examples of fitted trend models involved in RK for RST

Date	Hour	Significant variables	Sign of Coefficients	R ²
11-18-2018	3 a.m.	Air temperature/Latitude/Altitude	(+)/(-)/(-)	81%
11-25-2018	7 a.m.	Longitude/Latitude/Altitude	(-)/(-)/(-)	92%
11-25-2018	6 p.m.	Altitude/Slope	(-)/(-)	53%
12-31-2018	2 p.m.	Air temperature/Longitude/Altitude	(+)/(-)/(-)	48%

By inspecting the signs of the coefficients, the calibration results for the air temperature (AT) and geographical features make intuitive sense. For instance, RST is likely to be higher in the locations where AT is also higher. By contrast, RST decreases when the altitude value increases because the elevation of the study area became higher when moving toward the north. The same trend is observed for latitude as temperatures are known to decrease as latitude increases. Since the highway stretch isn't perfectly vertical, longitude, which measures the degree of continentality, was also found to have a negative relationship with RST. Slope, the measure of steepness or the degree of inclination of the horizontal plane, also has a negative relationship with RST as anticipated. Aspect, the compass direction that a slope faces, can also have a strong influence on temperature. This is because, in the afternoon, the sun's rays are coming from the west and, with a higher aspect in this direction, the pavement is more exposed directly to the sun, which leads to a higher RST (Bennie et al. 2008). Other than the presented examples, trend models were established for all hourly observations with sufficient data, and all signs intuitively made sense upon further investigation.

However, by comparing the R^2 value for each regression model, the researchers found that the predictive ability of the regression models varied dramatically. One possible reason for this could be the different weather events that cause random fluctuations in the RST. The shortfalls in RST estimations suggested that using a trend model (i.e., the MLR model) alone may not achieve the desired results, and, thus, the kriging method should be incorporated to further refine the model and improve its performance.

With all hourly semivariogram models constructed, RK was then adopted to estimate RST for all of the remaining locations in the study area. For this case study, only observations from the AVL system were used for interpolation, and the AVL data points at or near the same location as a stationary RWIS system were considered surrogate stationary RWIS readings. The main reasons for using observations from the AVL data points in lieu of RWIS readings were as follows: 1) the real RWIS stations sometimes had missing values and thus could not be used as control points; 2) doing so would isolate any variability or differences between the AVL and RWIS sensors while also providing observed values, which can be used for model performance comparisons, in between RWIS stations; and 3) the measurement mechanisms for the AVL system and stationary RWIS stations are different, so only using AVL data points that were at or closest to the RWIS stations removed any potential biases. As a result, the semivariogram model and point measurements were the only inputs used in the RK technique for RSC interpolation, and the remaining unconverted AVL data points were used to cross validate estimation accuracy.

To evaluate the feasibility of RK, AVL point measurements closest to each RWIS station were incrementally added (from one to three) to the road network to cross validate the estimation accuracy for RK. In the first simulation to cross validate the RK estimations, only one surrogate point measurement station (i.e., the AVL data point that was closest to ROSI4) was used as the observed data to estimate the rest of the road segment study area (unmonitored areas). In the second simulation, two surrogate stations represented by the AVL data points that were closest to ROSI4 and RDSI4 were used as observed data points in estimating all other unknown locations. The third and final simulation repeated the same procedure but added the AVL data point that was closest to RLEI4 as the additional data input. The cross-validation results of these examples are shown in Table 4-2.

Table 4-2. Examples of the fitted semivariogram models for RST

Date	Hour	Nugget	Range (m)	Sill	#inputs point measurements	RMSE	$\overline{\sigma^2}$
11-18-2018	3 a.m.	0.000	13,978.186	0.304	1	0.396	0.369
					2	0.377	0.277
					3	0.396	0.219
11-25-2018	7 a.m.	0.042	53,658.513	0.051	1	0.261	0.100
					2	0.242	0.075
					3	0.237	0.063
11-25-2018	6 p.m.	0.096	28,419.104	0.511	1	0.805	1.022
					2	0.713	0.767
					3	0.592	0.634

Date	Hour	Nugget	Range (m)	Sill	#inputs point measurements	RMSE	$\overline{\sigma^2}$
12-31-2018	2 p.m.	0.042	24,682.661	0.078	1	0.281	0.156
					2	0.28	0.117
					3	0.307	0.102

Table 4-2 shows that, overall, the RMSE value decreases as the number of point measurement inputs increases, and this can be observed on November 25, 2018 at 7 a.m. and November 25, 2018 at 6 p.m. However, this does not consistently happen for all hourly events, and one of the reasons for this can be attributed to the sampling locations of the point measurements (i.e., the existing RWIS station locations). Some locations provide inputs values that may not be as representative of distant areas as other locations; thus, local attributes of the data point will affect the overall estimation performance, especially if the locations have significantly different local attributes.

Different hourly weather events can be another reason for this phenomenon, as the temporal variation of meteorological factors tends to affect spatial structures of RSC as well. However, the kriging estimation variance does decrease with every additional station. This means that, by adding more stations, more variance is accounted for by the model, making it more reliable. Ultimately, this shows that adding stations requires an optimal placement strategy that incorporates local attributes and different weather events, which is a future research topic worth investigating.

The potential in the method developed and implemented here can be portrayed clearly by the comparisons between the estimated and the actual observed RST profiles depicted in Figure 4-1.

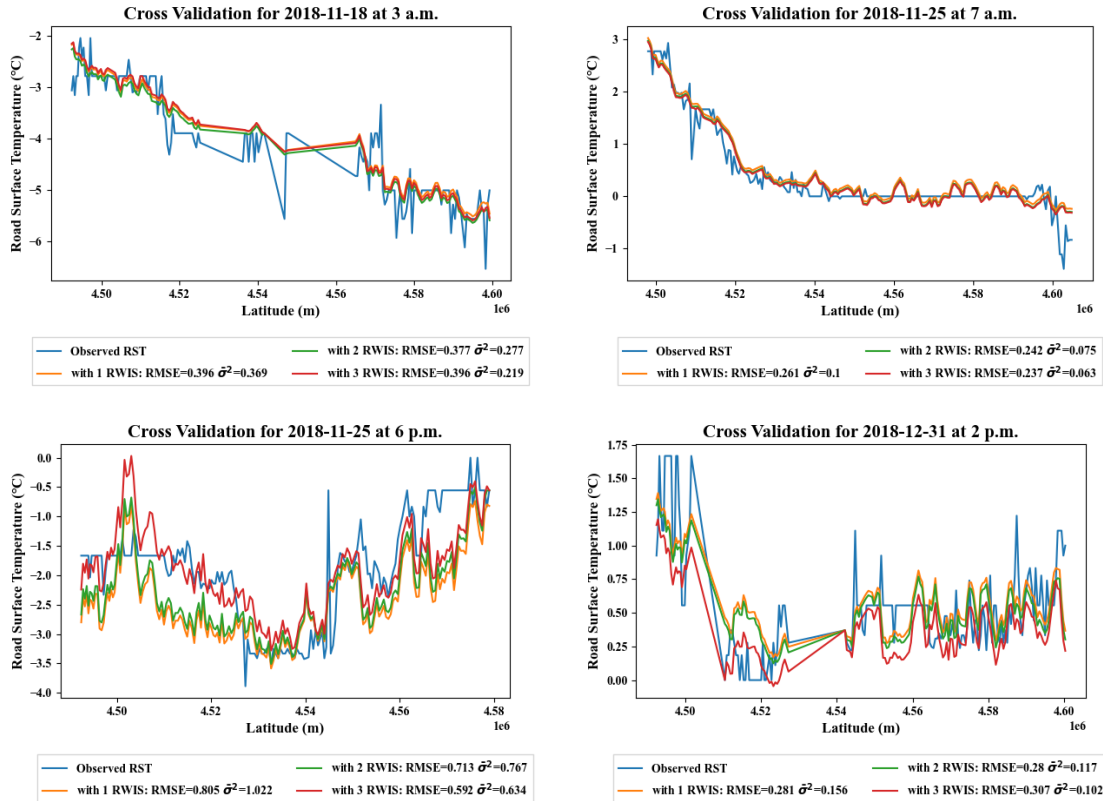


Figure 4-1. Examples of the RK estimated RST versus observed RST

Visual inspection of the four sample data sets confirmed that the RK model did well in capturing the general spatial variation pattern found in the observed data. The findings further showed that the proposed method needed as little as a single point measurement as input to fill in a large spatial gap that existed between RWIS stations.

To promote better visualization, the RST estimation results were illustrated using an interactive HTML-based web visualization tool. As shown in Figure 4-2, the tool offers a convenient way of visualizing the estimation results, including estimated values and estimation variances, with the freedom of choosing a different number of RWIS inputs and also their respective estimation accuracy.

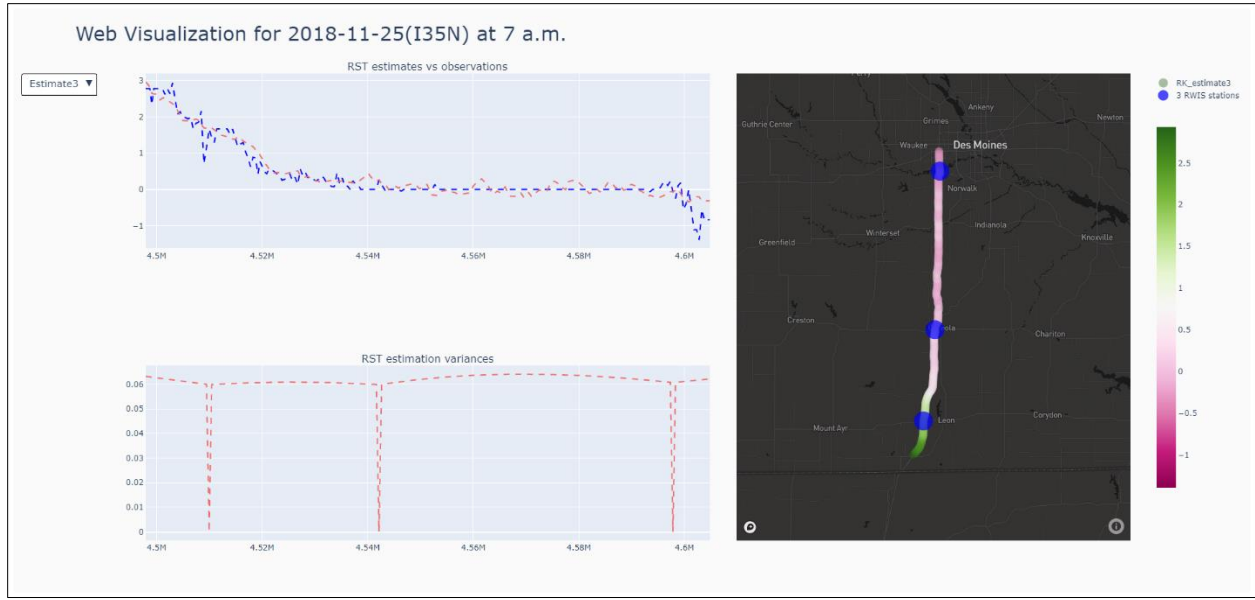


Figure 4-2. Example of the interactive web visualization tool for RST

4.2 Spatial Mapping of Road Surface Indices

To spatially map RSI, as previously illustrated in Figure 2-1, the researchers utilized both DL and RK. Given that the RSI values were not directly measured but collected using dash cameras from maintenance vehicles, the research team used the DL model to automate the process of in-vehicle RSC image recognition, and then converted the predicted RSC category to RSI values using an image thresholding technique, as discussed in this section. Finally, the RK model was adopted again to estimate RSI for the unvisited areas (i.e., locations where RSC images were not available).

4.2.1 Road Surface Condition Image Recognition via Deep Learning

Following the procedures described in the previous Methodology chapter, the DL model was developed using the TensorFlow application programming interface (API) (Abadi et al. 2016) and conducted with Compute Canada using a 32 GB graphics processing unit (GPU) (Baldwin 2012). Figure 4-3 shows the training and validation accuracy of the developed model, with a confusion matrix depicting the validation accuracy within each image classification group.

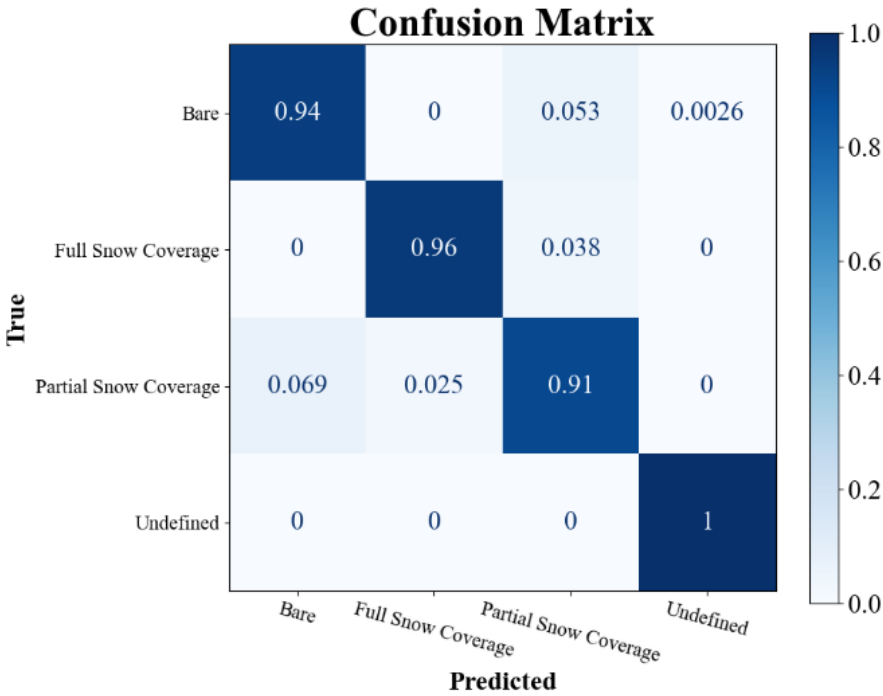
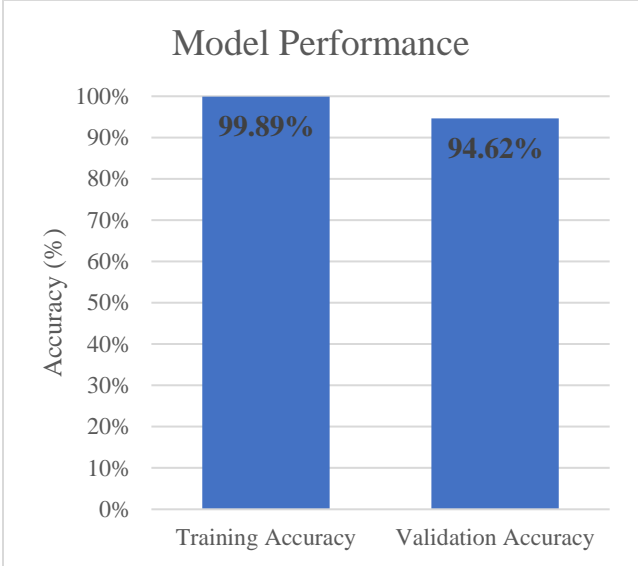


Figure 4-3. Deep learning model performance

The confusion matrix shows the performance of the DL model. The number of correct and incorrect predictions are summarized with normalized values (i.e., percentages) and are broken down by each category: bare pavement, partially snow covered, fully snow covered, and undefined. The values in the diagonal line of dark-shaded squares from upper left to lower right represent prediction accuracy, while the remaining values in the lighter-shaded squares in each column represent the false positive rate (FPR) (also known as a Type I error, where DL predictions are positive but they are false/incorrect predictions) and the values of each row represent the false negative rate (FNR) (also known as a Type II error, where DL predictions are negative but they are false/incorrect predictions).

For example, in the first row of the confusion matrix, 0.94 means the DL model correctly classified 94% of new bare pavement images into the Bare category, but incorrectly classified 0% (0), 5.3% (0.053), and 0.26% (0.0026) of them into the other three categories, and the summation of these three values is called the FNR. For other non-bare images, the DL model incorrectly classified 0% (0), 6.9% (0.069), and 0% (0) from each category to the Bare category, and the summation of these three values is called the FPR. High prediction accuracy with a low FNR and FPR implies an accurate DL model.

Results showed that the developed DL model achieved a high level of training and validation accuracy overall. The confusion matrix also implied that the model could successfully distinguish different RSC images, as the validation accuracy for each category was over 90%. The researchers were able to conclude that the developed DL model can recognize RSC images quite accurately. The next step was to convert this direct measure of RSC into a numerical value, RSI, for continuous spatial mapping.

4.2.2 Road Surface Index Conversion

The RSC category obtained using the DL model is a discrete measure representing the amount of snow coverage (bare pavement, partly snow covered, or fully snow covered) on the road surface, which cannot be conveniently used for spatial inference. As a result, the researchers adopted an approach proposed by Fu et al. (2017) to map the RSC categories to a continuous measure called the RSI, as shown in Table 4-3.

Table 4-3. RSC categories and corresponding RSI values

Original				Customized (i.e., our case)
RSC Category	Road Surface Index (RSI)			RSC Category
	Min.	Max.	Avg.	
Bare and Dry	0.9	1	0.95	Bare Pavement
Bare and Wet	0.8	0.9	0.85	
Slushy	0.7	0.8	0.75	Partially Snow Covered
Partly Snow Covered	0.5	0.7	0.6	
Snow Covered	0.3	0.5	0.4	Fully Snow Covered
Snow Packed	0.2	0.3	0.25	
Icy	0.05	0.2	0.125	N/A

The seven original RSC categories are listed above and in the leftmost column of the table. This study used only three categories, as listed in the rightmost column of the table. It is important to note that if the camera image is classed as fully snow covered, it cannot distinguish between packed or unpacked snow; for this reason, they are grouped together. Additionally, the icy category is omitted in this case study as the RSI value is developed using conventional camera

technology, making it impossible to identify icy road surfaces. Details of the RSI with regard to each RSC category are summarized in Table 4-3.

Given that the customized RSC categories shown in the rightmost column of Table 4-3 are based on one-to-one mapping, using one single value (e.g., mean value of the included original RSC categories) to represent each customized RSC category will inevitably eliminate a lot of details. For example, in the image labeling process, pavements with one wheel path visible, two-wheel paths visible, etc. are all labeled into the partially snow-covered category; however, their degree of slipperiness can be very different. To solve this issue, an image thresholding technique was adopted (Sezgin and Sankur 2004, Dawson-Howe 2014).

Image thresholding is a simple form of image segmentation. It is a non-linear operation that converts a gray-scale image into a binary image where two levels are assigned to the pixels depending on whether they are below or above the specified threshold value. In other words, if the pixel value is greater than the threshold, it is assigned one value (white). If not, it is assigned the other value (black).

After separating each partially snow covered image into foreground values (with black representing visible pavement) and background values (with white representing snow and/or ice), the proportion of background values in each image can be used to adjust the RSI values found in Table 4-3. For example, the adjusted RSI of a partially snow covered pavement with 60% background values can be obtained as $0.8 - (0.8 - 0.5) \times 60\% = 0.62$.

In our case, an adaptive thresholding algorithm was adopted to calculate thresholds for small regions of each image, so that different thresholds can be generated in different regions of the same image under varying light conditions. In addition, to eliminate bias caused by unnecessary features within the image (e.g., vehicle headlights, roadside vegetation) prior to the image thresholding process, each image is cropped to a relatively small extent to represent the pavement conditions in the primary driving lane. An example of these two processes is depicted in Figure 4-4.



Figure 4-4. Example of image cropping and thresholding process

The other two RSC categories (i.e., bare pavement and fully snow covered) are uniformly converted to the mean values of each RSI range (0.9 and 0.35, respectively) as the snow status in these two categories are technically almost the same. All RSC images were converted to their RSI values following the same procedures, and descriptive statistics for the converted RSI values can be found in the previous Table 3-2.

4.2.3 Road Surface Index Interpolation

With the developed DL model, the RSI values can be obtained from the images following the image thresholding procedures described in the previous section. Then, to spatially interpolate the RSI values, RK is adopted again, except, in this case, the trend removal uses a second-order polynomial curve. Examples of trend removal results and cross validation with incremental point measurements as input are shown in Table 4-4, Table 4-5, and Figure 4-5.

Table 4-4. Examples of trend removal results involved in RK for RSI

Date	Hour	Significant variables	Sign of Coefficients	R ²
11-25-2018	10 a.m.	Altitude ²	(-)	56%
1-12-2019	1 a.m.	Altitude/Altitude ²	(+)/(-)	32%
1-12-2019	8 a.m.	Altitude	(-)	21%
1-18-2019	8 p.m.	Altitude ²	(-)	37%

Table 4-5. Examples of the fitted semivariogram models for RSI

Date	Hour	Nugget	Range (m)	Sill	#inputs point measurements	RMSE	$\overline{\sigma^2}$
11-25-2018	10 a.m.	0.019	52,330.546	0.019	1	0.151	0.037
					2	0.152	0.027
					3	0.146	0.023
1-12-2019	1 a.m.	0.010	30,676.037	0.018	1	0.160	0.033
					2	0.158	0.023
					3	0.179	0.019
1-12-2019	8 a.m.	0.007	35,581.762	0.015	1	0.140	0.026
					2	0.128	0.018
					3	0.116	0.015
1-18-2019	8 p.m.	0.009	55,272.873	0.009	1	0.100	0.017
					2	0.154	0.013
					3	0.132	0.011

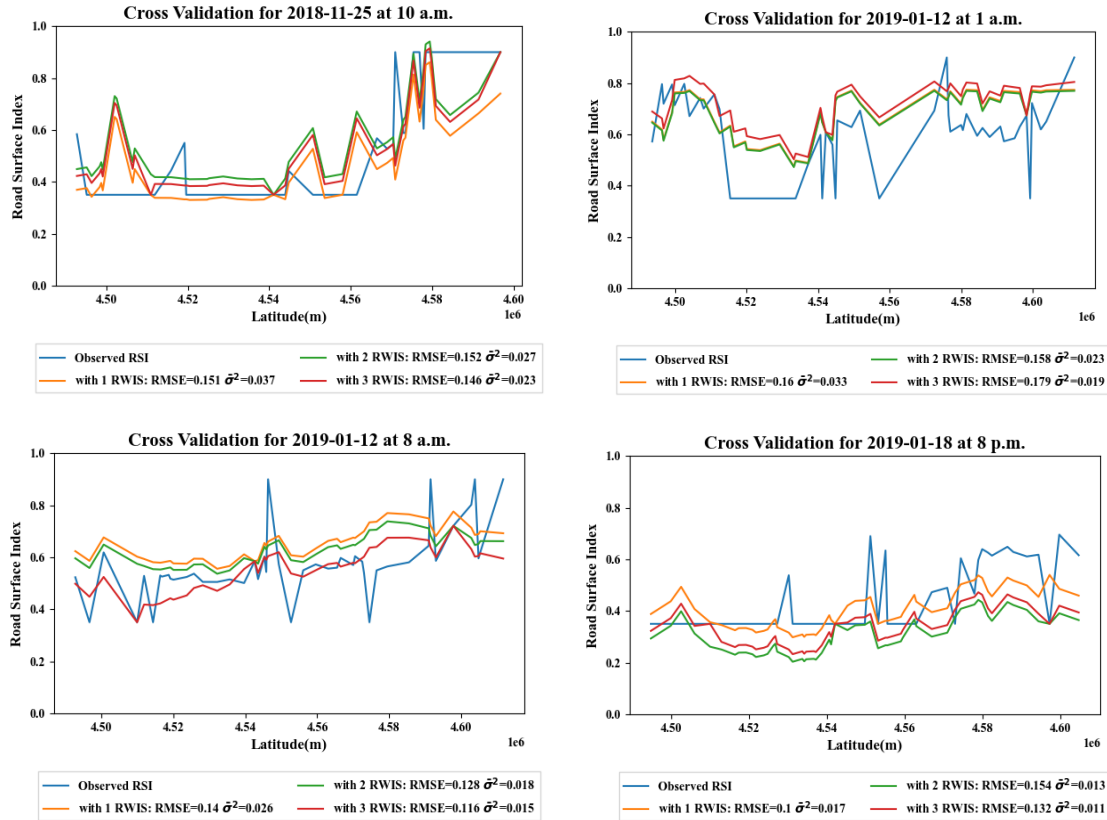


Figure 4-5. Examples of the RK estimated RSI versus observed RSI

Again, the same four examples are shown in this section for illustration purposes, and the complete results are included in Appendix B.

The results indicated that the general pattern of RSI along the highway stretch can also be well captured by the proposed method, even with as few as one RWIS point measurement as input. The findings for RSI estimation are very similar to what was discussed for the RST analysis, in that the estimation accuracy does not consistently improve with an increasing number of data points as input. However, also much like the results from the RST analysis, every additional station does in fact provide additional benefit to the kriging estimation variance (i.e., uncertainty) in how it decreases with every additional station.

Minimizing uncertainty in spatial inference is particularly important for winter maintenance personnel as operations-related decisions should be made using more reliable condition estimates. To maximize the monitoring and estimation return from a limited number of RWIS stations, efforts are needed to choose appropriate sites to install RWIS stations by considering local attributes and different weather conditions. This helps ensure that the system can produce the most accurate information about various hazardous events to help transportation agencies make more informed decisions in a strategic RWIS network planning process (Kwon et al. 2015, Biswas et al. 2019).

Another phenomenon observed that warrants further discussions is that the converted RSI values, as shown in the previous Figure 4-5, still have severe fluctuations at some locations with several possible causes for this. It could be a result of a lack of data points (i.e., the collected RSC images, which have limited spatial coverage). It can also be a result of the image translation to RSI valuation. Given that the image is converted for thresholding analysis (pixel proportions), it can be highly susceptible to extraneous features in the image such as vegetation or highly reflective surfaces.

To further improve it, a finer scale of RSI conversion can be one of the possible solutions to determine a more representative RSI value for each RSC category, so that a more representative pattern of the actual road conditions can be reflected. The addition of a thermal camera may also provide an additional source of image information that may make the RSI translation more accurate. As a final suggestion, the inclusion of a friction sensor may also aid in the determination of the RSI values, as it can detect icy roads and will better determine how slippery the roads actually are.

Nevertheless, the findings reported herein provide significant contributions to the advancement of our understanding as well as the methodology for inferring large spatial gaps with limited point measurements.

Lastly, the similar interactive visualization tool developed for RST was also made available for RSI as shown in Figure 4-6.

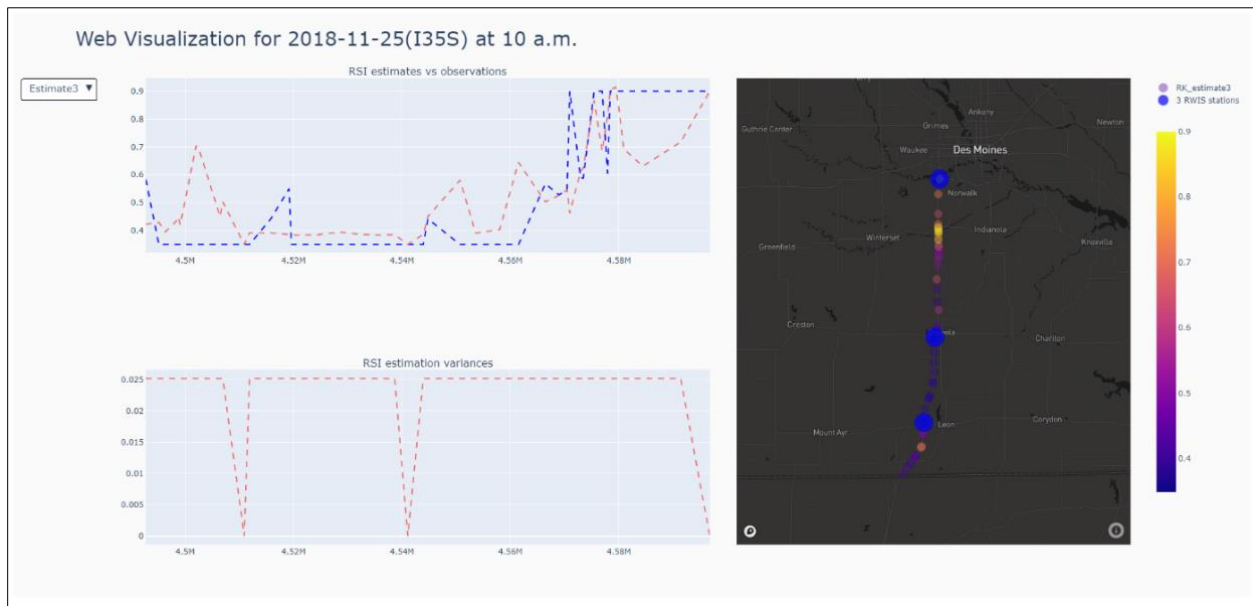


Figure 4-6. Example of the interactive web visualization tool for RSI

The figure well portrays the excellence of the proposed hybrid method that can accurately estimate road slipperiness over a long stretch of highway using limited inputs.

4.3 Weather Events Characterization

In addition to interpolating the RSC variables, it is also important to understand the spatial variation pattern with respect to meteorological factors. These findings can be used as priori knowledge for implementing RK without sending AVL trucks to collect data before making decisions on WRM activities. Since the available number (i.e., 34) of hourly events with RSI values was not enough to make a generalized result, only RST observations were included in this portion of the study.

The NSR, which represents the spatial dependence of the target variable within the study area, was used to characterize the spatial dependence of the RST. This value can vary a lot with different weather events. Guided by the literature review and data availability, wind and rainfall were used in this study to examine the potential correlations between RST and these weather events themselves. All variables regarding these two weather events were aggregated into the three NSR classes (i.e., the spatial dependence classes of strong [$NSR \leq 25\%$], moderate [$25\% < NSR < 75\%$], and weak [$NSR \geq 75\%$]). Furthermore, to test to see if patterns also existed in different time periods, all the observation months were split into shoulder months (October 2018, November 2018, March 2019, and April 2019) and typical winter months (December 2018, January 2019, and February 2019). The results and interpretations for these two meteorological factors are presented in the following subsections.

4.3.1 Wind

As previously described, four wind-related factors were involved in examining the correlations against RST spatial dependence using NSR classes. The plots in Figure 4-7 reveal an expected pattern.

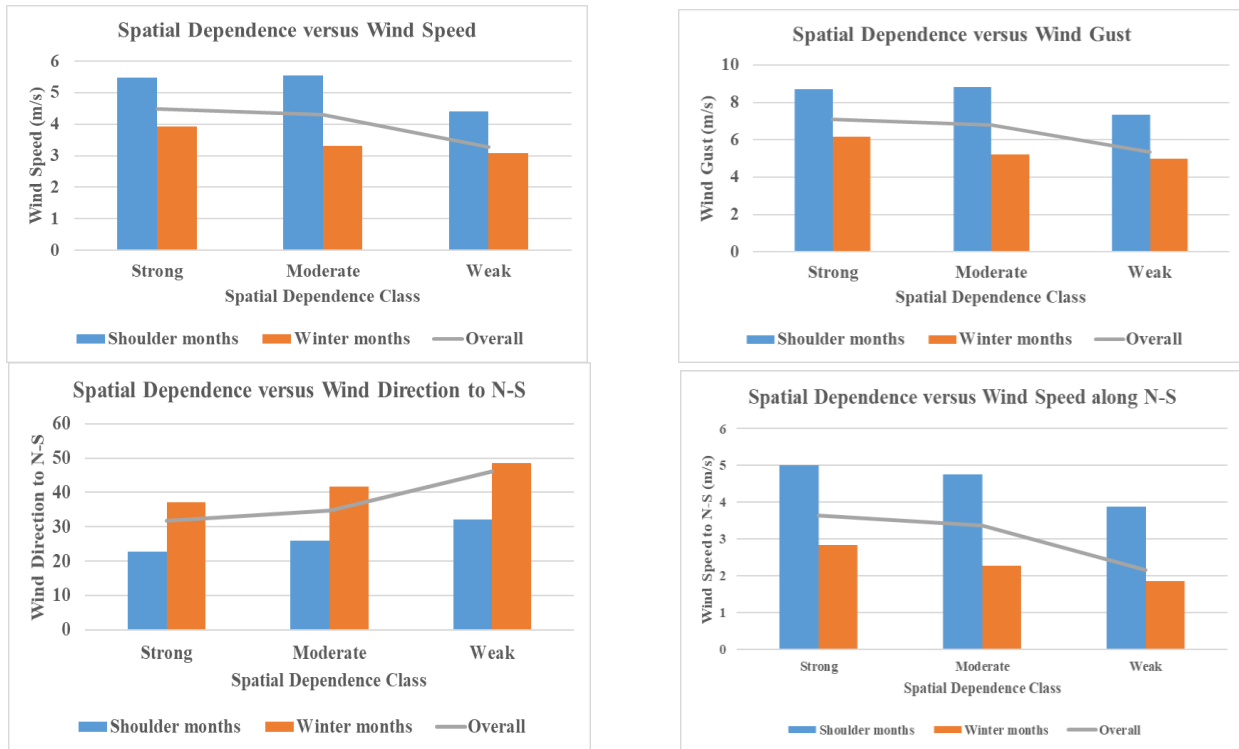


Figure 4-7. Relationship between spatial dependence and wind-related factors

By looking at the results, the researchers concluded that, in general, stronger winds tend to form stronger spatial dependencies within RST. Wind gust and wind speed along the north-to-south direction are both positively correlated with spatial dependence, with the wind speed relationship being the most evident. Paired *t*-tests statistically proved that, among the four wind-related factors, the difference between the strong and weak class and the difference between the moderate and weak class are significant, while there is no significance between the difference between the strong and moderate class during the shoulder months. Stronger winds can prevent the stabilization and inversion of RST, making them more correlated with each other along the roadway. The wind direction angle relative to the north-to-south direction also affects spatial dependence, with winds closer to the direction of the roadway resulting in stronger RST spatial dependence.

4.3.2 Rainfall

Similarly, the same examination methods were conducted to compare the potential relationship between rainfall intensity and RST spatial dependence. The results are shown in Figure 4-8.

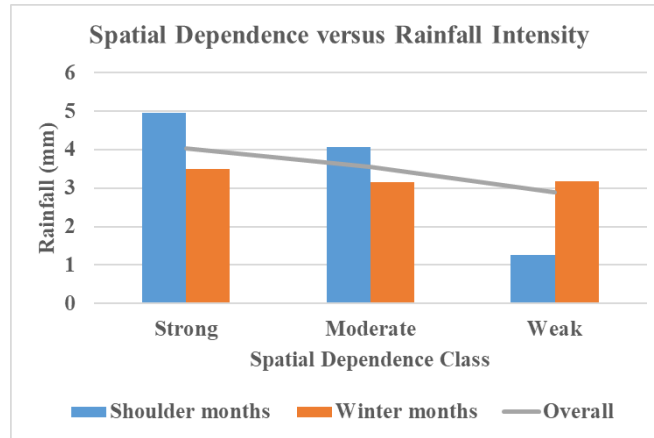


Figure 4-8. Relationship between spatial dependence and rainfall intensity

Overall, heavier rainfall tended to create stronger RST spatial dependence in the study area. This is intuitive as heavier rainfall cools down nearby surface air, reducing the random temperature variations along the roadway. This observed pattern was similar between the shoulder months and winter months. However, given that Iowa winters are often very dry with rare rainfall events, the pattern frequency will likely differ. Statistical *t*-tests using the 90% confidence intervals showed similar results, and different levels of rainfall intensities differed significantly among all spatial dependence classes for the shoulder months with the lone exception of the strong and moderate class, whose differences were found to be insignificant during both the winter and shoulder months. The reason for this can be explained by the limited rainfall observations, especially during the winter season.

Given that weather events are such complex entities, analyzing an individual meteorological factor typically requires long-term observations and a large sample size (Lundquist and Cayan 2007, Bogren et al. 2000). In this study, the only available data were from a single season; therefore, the research team lacked sufficient data to generate more conclusive results. In addition, the mutual effects between different meteorological factors can also influence RST variations (Gustavsson 1990, Postgård and Lindqvist 2001, FHWA 2020), which makes comparisons even more difficult.

5. CONCLUSION AND RECOMMENDATIONS

Estimating RSC has long been recognized as a challenging task, while it is essential in optimizing WRM operations. This project aimed to help address this challenge by utilizing data from two types of RWISs that have gained popularity for their ability to help monitor winter RSCs. With the RSC data garnered from RWIS stations and mobile units as inputs, several advanced modeling techniques can be applied to estimate the RSCs for unmeasured locations.

Through cross validation, the estimated RSC variables (i.e., RST and RSI) using RK showed excellent results, confirming the feasibility of the proposed method. With as few as one point measurement as input, RK can well capture the general patterns of the RSC along a stretch of highway. The researchers also found that the estimation quality depends on the density of the RWIS network. They found that the accuracy of the developed model improves when the number of point measurements increases. This was further supported by kriging estimation variance, where it decreases with the addition of more RWIS stations, meaning the reliability of the model's predictions improves with the number of stations.

Contrary to this pattern, some hourly events showed that estimation errors (i.e., RMSE) did not decrease with an increased number of input point measurements, which can be attributed to different weather events affecting the RK interpolation accuracy, as it is not typically uniform over space or time. This also suggested that an optimal placement strategy for RWIS stations is needed to account for both local and regional weather characteristics.

To automate the process of RSC image recognition, a DL model was developed. Its associated high training and validation accuracy proved its effectiveness in determining RSC via images collected from vehicle-mounted dash cameras. However, the researchers found limitations to this DL model, in that it is constructed with a relatively simple architecture fit only for this project's specific purpose. It was also highly dependent on image quality given that images with extraneous elements tend to not be accurately classified.

Furthermore, weather events can be characterized by RST using the NSR. In general, the spatial dependence of RST becomes stronger with stronger wind and heavier rainfall. This result can help in understanding the correlation between the RST variation pattern and meteorological factors, which can also be used as priori knowledge for a more efficient RK interpolation and decision-making process for WRM activities.

In terms of future research, it is necessary to expand the case study area to cover more highway sections and other road types to further validate the proposed RK method, and to better generalize the weather characterization results. Additional variables, such as meteorological factors, geographical and topographical factors, and traffic parameters (e.g., traffic volumes) can be added into the analysis to minimize their potential confounding effects on the RSC.

To improve the generalization of RSC image recognition, more advanced DL models (e.g., ResNet-50) can be adopted to improve RSC image recognition performance. In addition, more

RSC categories can also be considered to further distinguish the differences between road surface slipperiness. Other computer vision or image processing techniques can also be developed and applied to convert each RSC image or RSC category into finer RSI values. Furthermore, the development and inclusion of better image technology, such as thermal camera overlays, have the potential to further improve RSC monitoring and estimation results.

Lastly, to better aid the decision-making process for WRM activities, the application of the RWIS location optimization method can be further extended to determine the optimal number of new RWIS stations required. Their corresponding optimal locations should also be considered by running multiple simulations and incorporating various objectives (e.g., traffic monitoring), weather events, and specific local attributes.

Using the techniques presented in this report, transportation agencies can expand their RSC spatial coverage substantially, enhancing their ability to perform WRM activities faster, more efficiently, and more cost-effectively, and ultimately provide the general public with a greater level of service in terms of winter traffic safety and mobility.

REFERENCES

- Abadi, M., P. Barham, J. Chen, Z. Chen, A. Davis, J. Dean, M. Devin, S. Ghemawat, G. Irving, M. Isard, M. Kudlur, J. Levenberg, R. Monga, S. Moore, D. G. Murray, B. Steiner, P. Tucker, V. Vasudevan, P. Warden, M. Wicke, Y. Yu, and X. Zheng. 2016. TensorFlow: A System for Large-Scale Machine Learning. 12th USENIX Symposium on Operating Systems Design and Implementation (OSDI) '16, November 2–4, Savannah, GA, pp. 265–283.
- Agarwal, M., T. H. Maze, and R. Souleyrette. 2005. Impacts of Weather on Urban Freeway Traffic Flow Characteristics and Facility Capacity. *Proceedings of the 2005 Mid-Continent Transportation Research Symposium*, August 18–19, Ames, IA. pp. 18–19.
- Armstrong, M. 1998. *Basic Linear Geostatistics*. Springer-Verlag Berlin Heidelberg.
- Baldwin, S. 2012. Compute Canada: Advancing Computational Research. *Journal of Physics: Conference Series*, Vol. 341, pg. 012001.
- Behrens, T., R. A. Rossel, R. Kerry, R. MacMillan, R., K. Schmidt, J. Lee, T. Scholten, and A.-X. Zhu. 2019. The Relevant Range of Scales for Multi-Scale Contextual Spatial Modelling. *Scientific Reports*, Vol. 9, No. 14800, pp. 1–9.
- Bennie, J., B. Huntley, B., A. Wiltshire, M. O. Hill, and R. Baxter. 2008. Slope, Aspect and Climate: Spatially Explicit and Implicit Models of Topographic Microclimate in Chalk Grassland. *Ecological Modelling*, Vol. 216, No. 1, pp. 47–59.
- Biswas, S., M. Wu, S. J. Melles, and T. J. Kwon. 2019. Use of Topography, Weather Zones, and Semivariogram Parameters to Optimize Road Weather Information System Station Density across Large Spatial Scales. *Transportation Research Record: Journal of the Transportation Research Board*, Vol. 2673, No. 12, pp. 301–311.
- Bogren, J., T. Gustavsson, and U. Postgård. 2000. Local Temperature Differences in Relation to Weather Parameters. *International Journal of Climatology: A Journal of the Royal Meteorological Society*, Vol. 20, No. 2, pp. 151–170.
- Bohling, G. 2005. Introduction to Geostatistics and Variogram Analysis. *Kansas Geological Survey*, pp. 1–20.
- Boselly, S. E. 2001. *NCHRP Project 20-7(117): Benefit/Cost Study of RWIS and Anti-Icing Technologies*. National Cooperative Highway Research Program, Washington, DC.
- Buchanan, F. and S. E. Gwartz. 2005. Road Weather Information Systems at the Ministry of Transportation, Ontario. 2005 Annual Conference of the Transportation Association of Canada, September 18–21, Calgary, AB.
- Cambardella, C. A., T. B. Moorman, J. M. Novak, T. B. Parkin, D. L. Karlen, R. F. Turco, and A. E. Konopka. 1994. Field-Scale Variability of Soil Properties in Central Iowa Soils. *Soil Science Society of America Journal*, Vol. 58, No. 5, pp. 1501–1511.
- Carrillo, J., M. Crowley, G. Pan, and L. Fu. 2019. Comparison of Deep Learning Models for Determining Road Surface Condition from Roadside Camera Images and Weather Data. Transportation Association of Canada and ITS Canada 2019 Joint Conference and Exhibition, September 22–26, Halifax, NS.
- Chapman, L., J. E. Thornes, and A. V. Bradley. 2001a. Modelling of Road Surface Temperature From a Geographical Parameter Database. Part 1: Statistical. *Meteorological Applications*, Vol. 8, No. 4, pp. 409–419.
- . 2001b. Modelling of Road Surface Temperature From a Geographical Parameter Database. Part 2: Numerical. *Meteorological Applications*, Vol. 8, No. 4, pp. 421–436.

- Cressie, N. 1990. The Origins of Kriging. *Mathematical Geology*, Vol. 22, No. 3, pp. 239–252.
- . 2015. *Statistics for Spatial Data*. John Wiley and Sons.
- Curran, P. J. 1988. The Semivariogram in Remote Sensing: An Introduction. *Remote Sensing of Environment*, Vol. 24, No. 3, pp. 493–507.
- Dahl, G. E., T. N. Sainath, and G. E. Hinton. 2013. Improving Deep Neural Networks for LVCSR Using Rectified Linear Units and Dropout. 2013 IEEE International Conference on Acoustics, Speech and Signal Processing, May 26–31, Vancouver, BC, pp. 8609–8613.
- Dawson-Howe, K. 2014. *A Practical Introduction to Computer Vision With OpenCV*. John Wiley and Sons.
- ESRI. 2011. ArcGIS Desktop Release 10. 2011. Environmental Systems Research Institute, Redlands, CA. pp. 437, 438.
- FHWA. 2020, February 20. *How Do Weather Events Impact Roads?* Federal Highway Administration, Washington, DC. Retrieved April 15, 2021, from FHWA Road Weather Management Program: https://ops.fhwa.dot.gov/weather/q1_roadimpact.htm.
- Fu, L., L. Thakali, T. J. Kwon, and T. Usman. 2017. A Risk-Based Approach to Winter Road Surface Condition Classification. *Canadian Journal of Civil Engineering*, Vol. 44, No. 3, pp. 182–191.
- Gal, Y. and Z. Ghahramani. 2016. Dropout as a Bayesian Approximation: Representing Model Uncertainty in Deep Learning. *Proceedings of the 33rd International Conference on Machine Learning*, Vol. 48, pp. 1050–1059.
- Goodwin, L. C. and P. A. Pisano. 2004. Weather-Responsive Traffic Signal Control. *ITE Journal*, Vol. 74, No. 6, pp. 28–33.
- Goovaerts, P. 1997. *Geostatistics for Natural Resources Evaluation*. Oxford University Press on Demand.
- Gu, L., M. Wu, and T. J. Kwon. 2019. An Enhanced Spatial Statistical Method for Continuous Monitoring of Winter Road Surface Conditions. *Canadian Journal of Civil Engineering*, Vol. 47, No. 10, pp. 1154–1165.
- Gustavsson, T. 1990. Variation in Road Surface Temperature Due to Topography and Wind. *Theoretical and Applied Climatology*, Vol. 41, No. 4, pp. 227–236.
- Hamori, S., M. Kawai, T. Kume, Y. Murakami, and C. Watanabe. 2018. Ensemble Learning or Deep Learning? Application to Default Risk Analysis. *Journal of Risk and Financial Management*, Vol. 11, No. 1, pg. 12.
- Hengl, T., G. Heuvelink, and D. Rossiter. 2007. About Regression-Kriging: From Theory to Interpretation of Results. *Computers and Geosciences*, Vol. 33, No. 10, pp. 1301–1315.
- Hengl, T., G. Heuvelink, and A. Stein. 2003. *Comparison of Kriging with External Drift and Regression Kriging*. International Institute for Geo-Information Science and Earth Observation (ITC), Enschede, The Netherlands.
- Jang, E., S. Gu, and B. Poole. 2016. Categorical Reparameterization with Gumbel-Softmax. *arXiv preprint arXiv:1611.01144*. Published as a conference paper at the 5th International Conference on Learning Representations, ICLR 2017, April 24–26, Toulon, France.
- Journel, A. G. and C. J. Huijbregts. 1978. *Mining Geostatistics*. Academic Press, London.
- Karl, J. W. and B. A. Maurer. 2010. Spatial Dependence of Predictions from Image Segmentation: A Variogram-Based Method to Determine Appropriate Scales for Producing Land-Management Information. *Ecological Informatics*, Vol. 5, No. 3, pp. 194–202.

- Khan, S., N. Islam, Z. Jan, I. U. Din, and J. J. Rodrigues. 2019. A Novel Deep Learning Based Framework for the Detection and Classification of Breast Cancer Using Transfer Learning. *Pattern Recognition Letters*, Vol. 125, pp. 1–6.
- Krige, D. G. 1981. *Lognormal-de Wijsian Geostatistics for Ore Evaluation*. South African Institute of Mining and Metallurgy, Johannesburg.
- Kwon, T. J. and L. Gu. 2017. Modelling of Winter Road Surface Temperature (RST) — A GIS-Based Approach. 2017 4th International Conference on Transportation Information and Safety (ICTIS), August 8–10, Banff, AB, pp. 551–556.
- Kwon, T. J., L. Fu, and C. Jiang. 2013. Effect of Winter Weather and Road Surface Conditions on Macroscopic Traffic Parameters. *Transportation Research Record: Journal of the Transportation Research Board*, No. 2329, pp. 54–62.
- . 2015. Road Weather Information System Stations — Where and How Many to Install: A Cost Benefit Analysis Approach. *Canadian Journal of Civil Engineering*, Vol. 42, No. 1, pp. 57–66.
- Kwon, T. J., L. Fu, and S. J. Melles. 2017. Location Optimization of Road Weather Information System (RWIS) Network Considering the Needs of Winter Road Maintenance and the Traveling Public. *Computer-Aided Civil and Infrastructure Engineering*, Vol. 32, No. 1, pp. 57–71.
- LeCun, Y., Y. Bengio, and G. Hinton. 2015. Deep Learning. *Nature*, Vol. 521, pp. 436–444.
- Ligas, M. and M. Kulczycki. 2010. Simple Spatial Prediction-Least Squares Prediction, Simple Kriging, and Conditional Expectation of Normal Vector. *Geodesy and Cartography*, Vol. 59, No. 2, pp. 69–81.
- Lundquist, J. D. and D. R. Cayan. 2007. Surface Temperature Patterns in Complex Terrain: Daily Variations and Long-Term Change in the Central Sierra Nevada, California. *Journal of Geophysical Research: Atmospheres*, Vol. 112, No. D11.
- Marchetti, M., L. Chapman, A. Khalifa, and M. Buès. 2014. New Role of Thermal Mapping in Winter Maintenance with Principal Components Analysis. *Advances in Meteorology*, Vol. 2014, Article 254795.
- Marchetti, M., M. Moutton, S. Ludwig, L. Ibos, V. Feuillet, and J. Dumoulin. 2011. Road Networks Winter Risk Estimation Using On-Board Uncooled Infrared Camera for Surface Temperature Measurements Over Two Lanes. *International Journal of Geophysics*, Vol. 2011, Article 514970.
- MTO. 1993–2009. *Ontario Road Safety Annual Reports*. Road Safety Policy Office – Vehicles, Safety Policy & Education Branch, Ministry of Transportation, Toronto, ON.
- Odeh, I., A. McBratney, and D. Chittleborough. 1995. Further Results on Prediction of Soil Properties from Terrain Attributes: Heterotopic Cokriging and Regression-Kriging. *Geoderma*, Vol. 67, No. 3–4, pp. 215–226.
- Olea, R. A. 2006. A Six-Step Practical Approach to Semivariogram Modeling. *Stochastic Environmental Research and Risk Assessment*, Vol. 20, No. 5, pp. 307–318.
- Oliver, M. A. and R. Webster. 1990. Kriging: A Method of Interpolation for Geographical Information Systems. *International Journal of Geographical Information Systems*, Vol. 4, No. 3, pp. 313–332.
- Pan, G., L. Fu, R. Yu, and M. Muresan. 2019. Evaluation of Alternative Pre-Trained Convolutional Neural Networks for Winter Road Surface Condition Monitoring. 2019 5th International Conference on Transportation Information and Safety (ICTIS), July 14–17, Liverpool, UK, pp. 614–620.

- Pan, G., M. Muresan, R. Yu, and L. Fu. 2020. Real-Time Winter Road Surface Condition Monitoring Using an Improved Residual CNN. *Canadian Journal of Civil Engineering*.
- Perchanok, M. 2002. Patchiness of Snow Cover and Its Relation to Quality Assurance in Winter Operations. In *New Challenges for Winter Road Service, XIth International Winter Road Congress*, January 28–31, Sapporo, Japan.
- Postgård, U. and S. Lindqvist. 2001. Air and Road Surface Temperature Variations During Weather Change. *Meteorological Applications: A Journal Of Forecasting, Practical Applications, Training Techniques and Modelling*, Vol. 8, No. 1, pp. 71–83.
- Sass, B. H. 1992. A Numerical Model for Prediction of Road Temperature and Ice. *Journal of Applied Meteorology and Climatology*, Vol. 31, No. 12, pp. 1499–1506.
- Sezgin, M. and B. Sankur. 2004. Survey Over Image Thresholding Techniques and Quantitative Performance Evaluation. *Journal of Electronic Imaging*, Vol. 13, No. 1, pp. 146–165.
- Shao, J., P. J. Lister, G. D. Hart, and H. B. Pearson. 1996. Thermal Mapping: Reliability and Repeatability. *Meteorological Applications*, Vol. 3, No. 4, pp. 325–330.
- Sokol, Z., V. Bližňák, P. Sedlák, P. Zacharov, P. Pešice, and M. Škuthan. 2017. Ensemble Forecasts of Road Surface Temperatures. *Atmospheric Research*, Vol. 187, pp. 33–41.
- Sun, X.-L., Q. Yang, H.-L. Wang, and Y.-J. Wu. 2019. Can Regression Determination, Nugget-to-Sill Ratio and Sampling Spacing? *Catena*, Vol. 181, Article 104092.
- Transport Association of Canada. 2003. *Salt Smart Train, The Trainer Program. Salt Smart Learning Guide*.
- Usman, T., L. Fu, and L. F. Miranda-Moreno. 2010. Quantifying Safety Benefit of Winter Road Maintenance: Accident Frequency Modeling. *Accident Analysis and Prevention*, Vol. 42, No. 6, pp. 1878–1887.
- Wang, M., S. Lu, D. Zhu, J. Lin, and Z. Wang. 2018. A High-Speed and Low-Complexity Architecture for Softmax Function in Deep Learning. 14th Asia Pacific Conference on Circuits and Systems (APCCAS), April 26–30, Chengdu, China, pp. 223–226.

APPENDIX A. RESULTS OF SPATIAL MAPPING OF ROAD SURFACE TEMPERATURE

Note that the following tables summarize the corresponding results involved in the steps of spatial mapping of RST, including fitting a trend model for RST, semivariogram model parameters and cross validation results.

Table A-1. Fitted trend models involved in RK for RST

Date	Hour	Driving Direction	Significant variables	Sign of coefficients	R ²
2018					
10-26	12 p.m.	I-35S	NA	NA	NA
11-7	1 p.m.	I-35N	Latitude	(-)	79%
11-8	10 a.m.	I-35N	Longitude	(-)	37%
11-8	10 a.m.	I-35S	Air/temperature/slope	(+)/(-)	10%
11-8	11 a.m.	I-35S	Latitude	(-)	13%
11-8	9 p.m.	I-35S	NA	NA	NA
11-8	8 a.m.	I-35N	Air/temperature	(+)	5%
11-8	9 a.m.	I-35N	Air/temperature/latitude	(+)/(-)	49%
11-8	9 a.m.	I-35S	Air/temperature/slope	(+)/(-)	13%
11-9	10 a.m.	I-35N	NA	NA	NA
11-9	9 a.m.	I-35N	NA	NA	NA
11-9	9 a.m.	I-35S	Longitude/altitude	(-)/(-)	39%
11-17	11 a.m.	I-35N	NA	NA	NA
11-17	12 p.m.	I-35S	NA	NA	NA
11-17	1 p.m.	I-35N	NA	NA	NA
11-17	1 p.m.	I-35S	Longitude/aspect	(-)/(+)	45%
11-17	2 p.m.	I-35N	Slope	(-)	2%
11-17	2 p.m.	I-35S	NA	NA	NA
11-17	3 p.m.	I-35N	Latitude/altitude	(-)/(-)	13%
11-17	3 p.m.	I-35S	Air/temperature/altitude/aspect	(+)/(-)/(+)	19%
11-17	4 p.m.	I-35N	Air/temperature	(+)	17%
11-17	4 p.m.	I-35S	Air/temperature	(+)	41%
11-17	5 p.m.	I-35N	NA	NA	NA
11-17	5 p.m.	I-35S	Air/temperature	(+)	18%
11-17	6 p.m.	I-35N	Air/temperature	(+)	19%
11-17	6 p.m.	I-35S	Longitude	(-)	11%
11-17	7 p.m.	I-35N	NA	NA	NA
11-17	7 p.m.	I-35S	Air/temperature/latitude	(+)/(-)	16%
11-17	8 p.m.	I-35N	Air/temperature	(+)	5%
11-17	8 p.m.	I-35S	NA	NA	NA
11-17	9 p.m.	I-35S	Air/temperature/latitude	(+)/(-)	48%

Date	Hour	Driving Direction	Significant variables	Sign of coefficients	R ²
11-17	10 p.m.	I-35N	Aspect	(+)	3%
11-17	10 p.m.	I-35S	Latitude	(-)	4%
11-17	11 p.m.	I-35N	NA	NA	NA
11-17	11 p.m.	I-35S	Air/temperature	(+)	3%
11-18	1 a.m.	I-35N	Latitude/altitude	(-)/(-)	50%
11-18	2 a.m.	I-35S	Air/temperature/latitude/altitude	(+)/(-)/(-)	85%
11-18	3 a.m.	I-35N	Air/temperature/longitude/latitude/altitude	(+)/(-)/(-)/(-)	88%
11-18	3 a.m.	I-35S	Air/temperature/longitude/latitude/altitude	(+)/(-)/(-)	81%
11-18	4 a.m.	I-35N	Air/temperature/altitude	(+)/(-)	73%
11-18	4 a.m.	I-35S	Air/temperature/latitude/altitude	(+)/(-)/(-)	75%
11-18	5 a.m.	I-35S	Latitude/altitude	(-)/(-)	46%
11-18	6 a.m.	I-35N	Latitude/altitude	(-)/(-)	49%
11-25	10 a.m.	I-35N	Air/temperature/latitude	(+)/(-)	68%
11-25	10 a.m.	I-35S	Air/temperature/latitude	(+)/(-)	42%
11-25	12 p.m.	I-35N	Air/temperature/longitude	(+)/(-)	55%
11-25	12 p.m.	I-35S	Air/temperature/latitude	(+)/(-)	44%
11-25	1 p.m.	I-35N	Air/temperature/longitude	(+)/(-)	62%
11-25	1 p.m.	I-35S	Air/temperature/latitude	(+)/(-)	62%
11-25	2 p.m.	I-35N	Altitude	(-)	27%
11-25	2 p.m.	I-35S	Air/temperature/latitude	(+)/(-)	35%
11-25	3 p.m.	I-35S	Altitude	(-)	44%
11-25	4 p.m.	I-35N	NA	NA	NA
11-25	5 p.m.	I-35S	Air/temperature/altitude	(+)/(-)	30%
11-25	6 p.m.	I-35N	Altitude/slope	(-)/(-)	53%
11-25	6 p.m.	I-35S	Longitude	(-)	9%
11-25	7 p.m.	I-35N	Air/temperature/altitude	(+)/(-)	51%
11-25	7 p.m.	I-35S	Air/temperature/latitude	(+)/(-)	22%
11-25	8 p.m.	I-35S	Air/temperature/Altitude	(+)/(-)	39%
11-25	9 p.m.	I-35S	Air/temperature/altitude	(+)/(-)	43%
11-25	10 p.m.	I-35N	Longitude/altitude/slope/aspect	(-)/(-)/(-)/(+)	58%
11-25	6 a.m.	I-35N	Air/temperature/longitude/altitude/slope/aspect	(+)/(-)/(-)/(-)/(+)	89%
11-25	6 a.m.	I-35S	Air/temperature/longitude/latitude/altitude/aspect	(+)/(-)/(-)/(-)/(+)	94%
11-25	7 a.m.	I-35N	Longitude/latitude/altitude	(-)/(-)/(-)	92%
11-25	7 a.m.	I-35S	Longitude	(-)	55%
11-25	8 a.m.	I-35N	Air/temperature/latitude/altitude	(+)/(-)/(-)	24%
11-25	8 a.m.	I-35S	Air/temperature/longitude/altitude	(+)/(-)/(-)	43%
11-25	9 a.m.	I-35N	Air/temperature/longitude/altitude/slope/aspect	(+)/(-)/(-)/(-)/(+)	41%
11-25	9 a.m.	I-35S	Air/temperature/longitude	(+)/(-)	65%
11-26	0 a.m.	I-35S	Altitude	(-)	62%
11-26	11 a.m.	I-35N	Longitude/altitude/slope	(-)/(-)/(-)	31%

Date	Hour	Driving Direction	Significant variables	Sign of coefficients	R ²
11-26	11 a.m.	I-35S	Longitude/altitude	(-)/(-)	20%
11-26	12 p.m.	I-35N	Air/temperature/latitude	(+)/(-)	72%
11-26	12 p.m.	I-35S	Longitude/altitude	(-)/(-)	31%
11-26	2 p.m.	I-35N	Longitude	(-)	11%
11-26	4 a.m.	I-35N	Altitude	(-)	45%
11-26	6 a.m.	I-35N	Latitude/altitude/slope	(-)/(-)/(-)	64%
11-26	8 a.m.	I-35S	Air/temperature/latitude/altitude	(+)/(-)/(-)	36%
11-27	11 a.m.	I-35N	Altitude/slope	(-)/(-)	38%
12-3	11 a.m.	I-35S	Altitude	(-)	52%
12-4	10 p.m.	I-35N	Air/temperature/altitude	(+)/(-)	6%
12-4	10 p.m.	I-35S	Air/temperature	(+)	8%
12-4	7 a.m.	I-35N	Longitude/altitude	(-)/(-)	48%
12-4	7 a.m.	I-35S	Longitude/altitude	(-)/(-)	31%
12-7	8 a.m.	I-35N	Air/temperature	(+)	24%
12-12	10 a.m.	I-35S	Air/temperature/longitude/latitude	(+)/(-)/(-)	69%
12-12	2 p.m.	I-35S	NA	NA	NA
12-12	8 a.m.	I-35N	NA	NA	NA
12-19	9 a.m.	I-35S	Latitude	(-)	87%
12-24	8 a.m.	I-35N	Air/temperature/longitude	(+)/(-)	68%
12-24	8 a.m.	I-35S	Air/temperature/latitude	(+)/(-)	80%
12-24	9 a.m.	I-35S	Air/temperature/longitude	(+)/(-)	36%
12-28	5 a.m.	I-35N	Altitude	(-)	21%
12-28	6 a.m.	I-35N	Altitude	(-)	5%
12-28	6 a.m.	I-35S	Latitude/altitude	(-)/(-)	24%
12-28	7 a.m.	I-35N	Latitude/altitude	(-)/(-)	20%
12-28	7 a.m.	I-35S	Altitude	(-)	-5%
12-31	1 p.m.	I-35S	Air/temperature/longitude/altitude	(+)/(-)/(-)	41%
12-31	2 p.m.	I-35N	Air/temperature/longitude/altitude	(+)/(-)/(-)	48%
12-31	2 p.m.	I-35S	Longitude	(-)	4%
12-31	3 p.m.	I-35N	Latitude/altitude	(-)/(-)	30%
12-31	3 p.m.	I-35S	Air/temperature/latitude	(+)/(-)	13%
12-31	4 p.m.	I-35S	Longitude	(-)	50%
2019					
1-11	6 p.m.	I-35N	Altitude	(-)	18%
1-11	6 p.m.	I-35S	Air/temperature/altitude	(+)/(-)	61%
1-11	7 p.m.	I-35N	Air/temperature/altitude	(+)/(-)	23%
1-11	7 p.m.	I-35S	NA	NA	NA
1-11	8 p.m.	I-35N	NA	NA	NA
1-11	8 p.m.	I-35S	Altitude	(-)	26%
1-11	9 p.m.	I-35N	NA	NA	NA

Date	Hour	Driving Direction	Significant variables	Sign of coefficients	R ²
1-11	9 p.m.	I-35S	Air/temperature/latitude/altitude	(+)/(-)/(-)	21%
1-11	10 p.m.	I-35N	NA	NA	NA
1-11	10 p.m.	I-35S	Air/temperature	(+)	8%
1-11	8 a.m.	I-35S	Latitude/altitude	(-)/(-)	71%
1-12	0 a.m.	I-35N	Air/temperature/latitude/slope	(+)/(-)/(-)	23%
1-12	0 a.m.	I-35S	Air/temperature/latitude	(+)/(-)	34%
1-12	10 a.m.	I-35N	Air/temperature	(+)	7%
1-12	10 a.m.	I-35S	Air/temperature	(+)	13%
1-12	11 a.m.	I-35N	Air/temperature	(+)	11%
1-12	12 p.m.	I-35S	Latitude	(-)	35%
1-12	2 p.m.	I-35N	NA	NA	NA
1-12	2 p.m.	I-35S	NA	NA	NA
1-12	3 p.m.	I-35N	Latitude	(-)	34%
1-12	4 p.m.	I-35N	Air/temperature/latitude	(+)/(-)	30%
1-12	4 p.m.	I-35S	Latitude/altitude	(-)/(-)	27%
1-12	5 p.m.	I-35N	Latitude	(-)	10%
1-12	5 p.m.	I-35S	Latitude/slope	(-)/(-)	10%
1-12	6 p.m.	I-35S	Latitude	(-)	14%
1-12	7 p.m.	I-35N	Latitude	(-)	22%
1-12	7 p.m.	I-35S	Latitude	(-)	29%
1-12	1 a.m.	I-35N	Slope	(-)	0%
1-12	1 a.m.	I-35S	Air/temperature/longitude/latitude/altitude	(+)/(-)/(-)/(-)	37%
1-12	8 p.m.	I-35N	Latitude	(-)	18%
1-12	8 p.m.	I-35S	Air/temperature/latitude	(+)/(-)	56%
1-12	9 p.m.	I-35N	Air/temperature/latitude	(+)/(-)	41%
1-12	9 p.m.	I-35S	Latitude	(-)	25%
1-12	2 a.m.	I-35N	Air/temperature	(+)	2%
1-12	2 a.m.	I-35S	Air/temperature/latitude	(+)/(-)	37%
1-12	3 a.m.	I-35N	Air/temperature/longitude/latitude/slope	(+)/(-)/(-)/(-)	45%
1-12	3 a.m.	I-35S	Air/temperature/latitude	(+)/(-)	19%
1-12	4 a.m.	I-35N	NA	NA	NA
1-12	4 a.m.	I-35S	Air/temperature/latitude	(+)/(-)	15%
1-12	5 a.m.	I-35N	Air/temperature/latitude	(+)/(-)	34%
1-12	5 a.m.	I-35S	Air/temperature/latitude	(+)/(-)	12%
1-12	6 a.m.	I-35N	Air/temperature	(+)	8%
1-12	6 a.m.	I-35S	Air/temperature/latitude	(+)/(-)	43%
1-12	7 a.m.	I-35S	Latitude	(-)	4%
1-12	8 a.m.	I-35N	NA	NA	NA
1-12	9 a.m.	I-35N	Latitude/altitude	(-)/(-)	16%
1-12	9 a.m.	I-35S	NA	NA	NA

Date	Hour	Driving Direction	Significant variables	Sign of coefficients	R ²
1-14	9 p.m.	I-35S	NA	NA	NA
1-14	10 p.m.	I-35S	NA	NA	NA
1-15	7 a.m.	I-35N	Longitude	(-)	3%
1-15	7 a.m.	I-35S	Longitude/aspect	(-)/(+)	16%
1-15	8 a.m.	I-35N	Air/temperature/longitude/altitude	(+)(-)(-)	77%
1-17	10 a.m.	I-35S	NA	NA	NA
1-17	9 a.m.	I-35N	Air/temperature/latitude/aspect	(+)(-)/(+)	64%
1-17	9 a.m.	I-35S	Air/temperature/longitude	(+)(-)	67%
1-18	3 p.m.	I-35N	Latitude	(-)	51%
1-18	3 p.m.	I-35S	Latitude	(-)	73%
1-18	4 p.m.	I-35N	Latitude	(-)	56%
1-18	4 p.m.	I-35S	Latitude/altitude	(-)(-)	61%
1-18	5 p.m.	I-35N	Latitude	(-)	63%
1-18	5 p.m.	I-35S	Latitude	(-)	23%
1-18	6 p.m.	I-35N	Longitude	(-)	35%
1-18	6 p.m.	I-35S	Latitude	(-)	39%
1-18	7 p.m.	I-35N	NA	NA	NA
1-18	8 p.m.	I-35N	Latitude	(-)	50%
1-18	8 p.m.	I-35S	Latitude	(-)	49%
1-18	9 p.m.	I-35N	Latitude/altitude	(-)(-)	43%
1-18	10 p.m.	I-35S	Latitude	(-)	4%
1-18	11 p.m.	I-35N	NA	NA	NA
1-19	0 a.m.	I-35N	Latitude	(-)	11%
1-19	0 a.m.	I-35S	NA	NA	NA
1-19	11 a.m.	I-35S	NA	NA	NA
1-19	1 p.m.	I-35S	NA	NA	NA
1-19	1 a.m.	I-35N	NA	NA	NA
1-19	1 a.m.	I-35S	NA	NA	NA
1-19	2 a.m.	I-35N	NA	NA	NA
1-19	3 a.m.	I-35N	NA	NA	NA
1-19	3 a.m.	I-35S	NA	NA	NA
1-19	4 a.m.	I-35N	Longitude/altitude	(-)(-)	7%
1-19	5 a.m.	I-35S	Latitude/altitude	(-)(-)	36%
1-19	6 a.m.	I-35N	NA	NA	NA
1-19	7 a.m.	I-35N	NA	NA	NA
1-19	7 a.m.	I-35S	NA	NA	NA
1-19	9 a.m.	I-35N	NA	NA	NA
1-19	9 a.m.	I-35S	NA	NA	NA
1-22	11 a.m.	I-35N	Longitude	(-)	39%
1-22	2 p.m.	I-35N	Air/temperature	(+)	25%

Date	Hour	Driving Direction	Significant variables	Sign of coefficients	R ²
1-22	2 p.m.	I-35S	Longitude	(-)	4%
1-22	3 p.m.	I-35N	Latitude	(-)	31%
1-22	3 p.m.	I-35S	Latitude	(-)	26%
1-22	4 p.m.	I-35N	Air/temperature/latitude	(+)/(-)	52%
1-22	4 p.m.	I-35S	Latitude	(-)	37%
1-22	5 p.m.	I-35N	Latitude	(-)	54%
1-22	6 p.m.	I-35S	Latitude	(-)	41%
1-22	7 p.m.	I-35N	Latitude	(-)	37%
1-22	8 p.m.	I-35S	Latitude	(-)	15%
1-22	9 p.m.	I-35N	Air/temperature	(+)	10%
1-22	10 p.m.	I-35S	NA	NA	NA
1-22	7 a.m.	I-35N	Latitude	(-)	20%
1-22	7 a.m.	I-35S	Air/temperature	(+)	18%
1-22	8 a.m.	I-35N	Latitude	(-)	42%
1-22	8 a.m.	I-35S	Latitude	(-)	30%
1-22	9 a.m.	I-35S	Air/temperature	(+)	71%
1-23	0 a.m.	I-35S	Air/temperature	(+)	13%
1-23	1 a.m.	I-35S	NA	NA	NA
1-23	2 a.m.	I-35N	Air/temperature/longitude/latitude/altitude	(+)/(-)/(-)/(-)	56%
1-23	3 a.m.	I-35N	Altitude	(-)	-2%
1-23	3 a.m.	I-35S	Altitude/slope/aspect	(-)/(-)/(+)	1%
1-23	4 a.m.	I-35S	NA	NA	NA
1-23	6 a.m.	I-35N	Latitude/altitude	(-)/(-)	30%
1-23	6 a.m.	I-35S	NA	NA	NA
1-23	8 a.m.	I-35N	Latitude/altitude	(-)/(-)	36%
1-23	8 a.m.	I-35S	Latitude/altitude	(-)/(-)	17%
1-23	9 a.m.	I-35N	NA	NA	NA
2-4	1 p.m.	I-35S	Longitude/latitude	(-)/(-)	45%
2-5	2 p.m.	I-35N	Air/temperature/longitude/slope	(+)/(-)/(-)	50%
2-5	3 p.m.	I-35S	Longitude	(-)	15%
2-5	4 p.m.	I-35N	Latitude	(-)	17%
2-5	4 p.m.	I-35S	Latitude/altitude	(-)/(-)	52%
2-6	12 p.m.	I-35S	Latitude	(-)	45%
2-6	1 p.m.	I-35N	Latitude	(-)	51%
3-7	10 a.m.	I-35N	Longitude/latitude/altitude	(-)/(-)/(-)	82%
3-7	10 a.m.	I-35S	Longitude/latitude/altitude	(-)/(-)/(-)	80%
3-7	8 a.m.	I-35S	Longitude/latitude/altitude	(-)/(-)/(-)	79%
4-22	10 a.m.	I-35S	Altitude	(-)	32%

Table A-2. Fitted semivariogram models for RST

Date	Hour	Driving Direction	Nugget	Range (m)	Sill
2018					
10-26	12 p.m.	I-35S	0.051	11,958.308	1.372
11-7	1 p.m.	I-35N	0.310	35,966.653	1.760
11-8	10 a.m.	I-35N	0.234	41,126.960	0.466
11-8	10 a.m.	I-35S	0.046	8,847.762	0.295
11-8	11 a.m.	I-35S	0.096	15,605.738	0.272
11-8	9 p.m.	I-35S	0.064	61,591.321	0.302
11-8	8 a.m.	I-35N	0.124	11,374.337	0.151
11-8	9 a.m.	I-35N	0.017	18,433.231	0.297
11-8	9 a.m.	I-35S	0.099	27,231.494	0.547
11-9	10 a.m.	I-35N	0.196	54,424.761	0.546
11-9	9 a.m.	I-35N	0.105	36,909.671	0.483
11-9	9 a.m.	I-35S	0.000	15,226.424	0.478
11-17	11 a.m.	I-35N	0.031	32,846.856	0.056
11-17	12 p.m.	I-35S	0.029	28,823.151	0.098
11-17	1 p.m.	I-35N	0.030	48,381.545	0.109
11-17	1 p.m.	I-35S	0.011	51,751.486	0.026
11-17	2 p.m.	I-35N	0.000	24,143.907	0.044
11-17	2 p.m.	I-35S	0.007	54,911.166	0.036
11-17	3 p.m.	I-35N	0.000	7,771.192	0.012
11-17	3 p.m.	I-35S	0.008	37,135.255	0.045
11-17	4 p.m.	I-35N	0.010	32,000.997	0.069
11-17	4 p.m.	I-35S	0.012	27,161.786	0.056
11-17	5 p.m.	I-35N	0.008	10,607.947	0.071
11-17	5 p.m.	I-35S	0.069	44,777.273	0.153
11-17	6 p.m.	I-35N	0.000	24,402.719	0.248
11-17	6 p.m.	I-35S	0.089	22,791.375	0.194
11-17	7 p.m.	I-35N	0.000	14,628.645	0.257
11-17	7 p.m.	I-35S	0.000	24,613.146	0.395
11-17	8 p.m.	I-35N	0.047	31,166.606	0.311
11-17	8 p.m.	I-35S	0.017	17,577.484	0.407
11-17	9 p.m.	I-35S	0.000	9,016.454	0.240
11-17	10 p.m.	I-35N	0.000	27,187.638	0.454
11-17	10 p.m.	I-35S	0.155	47,559.992	0.540
11-17	11 p.m.	I-35N	0.000	35,359.017	1.125
11-17	11 p.m.	I-35S	0.001	12,424.344	0.361

Date	Hour	Driving Direction	Nugget	Range (m)	Sill
11-18	1 a.m.	I-35N	0.000	11,171.770	0.212
11-18	2 a.m.	I-35S	0.127	30,020.846	0.265
11-18	3 a.m.	I-35N	0.108	53,933.533	0.185
11-18	3 a.m.	I-35S	0.000	13,978.186	0.304
11-18	4 a.m.	I-35N	0.147	39,044.747	0.166
11-18	4 a.m.	I-35S	0.039	10,729.010	0.109
11-18	5 a.m.	I-35S	0.027	21,147.449	0.366
11-18	6 a.m.	I-35N	0.101	18,631.923	0.222
11-25	10 a.m.	I-35N	0.074	28,960.692	0.167
11-25	10 a.m.	I-35S	0.020	39,291.296	0.040
11-25	12 p.m.	I-35N	0.089	46,984.315	0.608
11-25	12 p.m.	I-35S	0.017	36,624.953	0.126
11-25	1 p.m.	I-35N	0.000	10,535.293	0.178
11-25	1 p.m.	I-35S	0.032	30,118.475	0.338
11-25	2 p.m.	I-35N	0.127	43,838.213	0.190
11-25	2 p.m.	I-35S	0.000	31,751.158	0.442
11-25	3 p.m.	I-35S	0.063	28,211.549	0.247
11-25	4 p.m.	I-35N	0.000	24,615.734	0.744
11-25	5 p.m.	I-35S	0.000	14,561.902	0.226
11-25	6 p.m.	I-35N	0.096	28,419.104	0.511
11-25	6 p.m.	I-35S	0.155	25,984.002	0.290
11-25	7 p.m.	I-35N	0.013	26,070.889	0.393
11-25	7 p.m.	I-35S	0.114	42,536.577	0.358
11-25	8 p.m.	I-35S	0.024	15,740.613	0.264
11-25	9 p.m.	I-35S	0.000	11,494.987	0.483
11-25	10 p.m.	I-35N	0.185	32,565.207	0.345
11-25	6 a.m.	I-35N	0.075	49,252.185	0.157
11-25	6 a.m.	I-35S	0.033	34,969.911	0.118
11-25	7 a.m.	I-35N	0.042	53,658.513	0.050
11-25	7 a.m.	I-35S	0.010	46,263.024	0.010
11-25	8 a.m.	I-35N	0.000	10,941.316	0.041
11-25	8 a.m.	I-35S	0.013	17,800.369	0.054
11-25	9 a.m.	I-35N	0.000	16,410.657	0.189
11-25	9 a.m.	I-35S	0.003	19,481.262	0.063
11-26	0 a.m.	I-35S	0.181	25,413.800	0.539
11-26	11 a.m.	I-35N	0.762	38,253.739	1.849
11-26	11 a.m.	I-35S	0.184	21,060.411	0.651
11-26	12 p.m.	I-35N	0.000	6,771.857	1.633

Date	Hour	Driving Direction	Nugget	Range (m)	Sill
11-26	12 p.m.	I-35S	0.002	17,311.313	1.557
11-26	2 p.m.	I-35N	0.396	50,707.929	0.971
11-26	4 a.m.	I-35N	0.013	20,697.856	0.611
11-26	6 a.m.	I-35N	0.059	36,787.176	0.256
11-26	8 a.m.	I-35S	0.000	16,315.187	1.100
11-27	11 a.m.	I-35N	0.453	50,124.616	0.899
12-3	11 a.m.	I-35S	0.078	14,498.589	0.136
12-4	10 p.m.	I-35N	0.059	10,312.636	0.120
12-4	10 p.m.	I-35S	0.030	10,141.927	0.126
12-4	7 a.m.	I-35N	0.088	15,374.602	0.169
12-4	7 a.m.	I-35S	0.088	16,924.546	0.175
12-7	8 a.m.	I-35N	0.044	11,056.439	0.618
12-12	10 a.m.	I-35S	0.272	25,569.979	0.638
12-12	2 p.m.	I-35S	0.370	23,815.205	0.652
12-12	8 a.m.	I-35N	0.008	40,592.349	0.054
12-19	9 a.m.	I-35S	0.000	16,224.347	0.315
12-24	8 a.m.	I-35N	0.226	32,127.789	0.491
12-24	8 a.m.	I-35S	0.019	8,743.662	0.302
12-24	9 a.m.	I-35S	0.062	42,354.415	0.253
12-28	5 a.m.	I-35N	0.034	18,662.358	0.337
12-28	6 a.m.	I-35N	0.060	19,367.030	0.347
12-28	6 a.m.	I-35S	0.056	25,494.080	0.245
12-28	7 a.m.	I-35N	0.084	39,760.539	0.648
12-28	7 a.m.	I-35S	0.000	51,878.246	0.436
12-31	1 p.m.	I-35S	0.043	37,286.521	0.065
12-31	2 p.m.	I-35N	0.042	24,682.661	0.078
12-31	2 p.m.	I-35S	0.005	19,812.657	0.206
12-31	3 p.m.	I-35N	0.042	44,858.235	0.051
12-31	3 p.m.	I-35S	0.103	34,591.615	0.108
12-31	4 p.m.	I-35S	0.028	7,391.895	0.069
2019					
1-11	6 p.m.	I-35N	0.016	17,828.126	0.026
1-11	6 p.m.	I-35S	0.017	40,117.781	0.021
1-11	7 p.m.	I-35N	0.004	12,942.280	0.005
1-11	7 p.m.	I-35S	0.003	40,117.781	0.003
1-11	8 p.m.	I-35N	0.000	42,056.932	0.000
1-11	8 p.m.	I-35S	0.000	20,779.439	0.038
1-11	9 p.m.	I-35N	0.023	2,439.208	0.023

Date	Hour	Driving Direction	Nugget	Range (m)	Sill
1-11	9 p.m.	I-35S	0.000	10,805.346	0.008
1-11	10 p.m.	I-35N	0.004	61611.974	0.004
1-11	10 p.m.	I-35S	0.005	53,420.979	0.005
1-11	8 a.m.	I-35S	0.061	37.390	0.063
1-12	0 a.m.	I-35N	0.031	28,918.797	0.248
1-12	0 a.m.	I-35S	0.000	19,260.806	0.184
1-12	10 a.m.	I-35N	0.021	43,230.283	0.075
1-12	10 a.m.	I-35S	0.000	8,317.595	0.042
1-12	11 a.m.	I-35N	0.005	44,263.670	0.005
1-12	12 p.m.	I-35S	0.000	52,108.606	0.254
1-12	2 p.m.	I-35N	0.084	56,040.403	0.412
1-12	2 p.m.	I-35S	0.017	26,989.937	0.307
1-12	3 p.m.	I-35N	0.037	61,390.778	0.468
1-12	4 p.m.	I-35N	0.007	54,428.692	0.056
1-12	4 p.m.	I-35S	0.024	52,221.455	0.069
1-12	5 p.m.	I-35N	0.002	56,627.964	0.003
1-12	5 p.m.	I-35S	0.000	12,965.825	0.091
1-12	6 p.m.	I-35S	0.000	19,722.426	0.281
1-12	7 p.m.	I-35N	0.044	61,615.509	0.175
1-12	7 p.m.	I-35S	0.023	56,867.566	0.092
1-12	1 a.m.	I-35N	0.000	15,957.429	0.126
1-12	1 a.m.	I-35S	0.016	41,942.636	0.244
1-12	8 p.m.	I-35N	0.043	51,393.142	0.165
1-12	8 p.m.	I-35S	0.014	53,921.407	0.029
1-12	9 p.m.	I-35N	0.009	26,303.517	0.037
1-12	9 p.m.	I-35S	0.010	61,646.963	0.042
1-12	2 a.m.	I-35N	0.000	28,273.347	0.133
1-12	2 a.m.	I-35S	0.108	52,632.815	0.201
1-12	3 a.m.	I-35N	0.081	47,466.667	0.164
1-12	3 a.m.	I-35S	0.033	41,806.368	0.154
1-12	4 a.m.	I-35N	0.000	21,707.843	0.263
1-12	4 a.m.	I-35S	0.053	33,857.080	0.293
1-12	5 a.m.	I-35N	0.107	40,968.285	0.361
1-12	5 a.m.	I-35S	0.000	27,467.551	0.512
1-12	6 a.m.	I-35N	0.061	27,134.475	0.231
1-12	6 a.m.	I-35S	0.049	36,966.970	0.359
1-12	7 a.m.	I-35S	0.193	312.524	0.239
1-12	8 a.m.	I-35N	0.000	22,015.210	0.199

Date	Hour	Driving Direction	Nugget	Range (m)	Sill
1-12	9 a.m.	I-35N	0.133	61,615.509	0.160
1-12	9 a.m.	I-35S	0.040	61,651.387	0.128
1-14	9 p.m.	I-35S	0.001	53,420.979	0.001
1-14	10 p.m.	I-35S	0.001	53,420.979	0.001
1-15	7 a.m.	I-35N	0.001	47,240.628	0.001
1-15	7 a.m.	I-35S	0.001	47,493.660	0.001
1-15	8 a.m.	I-35N	0.006	45,045.371	0.017
1-17	10 a.m.	I-35S	0.021	43,253.007	0.522
1-17	9 a.m.	I-35N	0.014	30,607.415	0.023
1-17	9 a.m.	I-35S	0.052	51,090.230	0.072
1-18	3 p.m.	I-35N	0.000	17,568.125	0.237
1-18	3 p.m.	I-35S	0.062	4,0267.539	0.266
1-18	4 p.m.	I-35N	0.059	25,751.923	0.354
1-18	4 p.m.	I-35S	0.163	61,651.387	0.203
1-18	5 p.m.	I-35N	0.061	24,118.295	0.293
1-18	5 p.m.	I-35S	0.134	28,239.908	0.314
1-18	6 p.m.	I-35N	0.000	23,133.923	0.569
1-18	6 p.m.	I-35S	0.044	41,966.192	0.646
1-18	7 p.m.	I-35N	0.123	28,757.519	0.450
1-18	8 p.m.	I-35N	0.000	36,377.646	0.993
1-18	8 p.m.	I-35S	0.000	29,919.393	0.934
1-18	9 p.m.	I-35N	0.279	320.177	0.409
1-18	10 p.m.	I-35S	0.000	22,775.763	0.821
1-18	11 p.m.	I-35N	0.000	50,492.153	0.677
1-19	0 a.m.	I-35N	0.000	16,561.519	1.041
1-19	0 a.m.	I-35S	0.000	33,036.641	1.240
1-19	11 a.m.	I-35S	0.000	48,231.128	5.520
1-19	1 p.m.	I-35S	0.677	50,981.737	1.192
1-19	1 a.m.	I-35N	0.000	12,891.462	0.648
1-19	1 a.m.	I-35S	0.284	56,863.120	0.534
1-19	2 a.m.	I-35N	0.321	51,908.604	0.392
1-19	3 a.m.	I-35N	0.000	21,559.645	1.383
1-19	3 a.m.	I-35S	0.237	61,651.387	0.364
1-19	4 a.m.	I-35N	0.131	24,938.996	1.193
1-19	5 a.m.	I-35S	0.001	14,249.759	0.342
1-19	6 a.m.	I-35N	0.000	27,263.761	1.475
1-19	7 a.m.	I-35N	0.378	61,611.974	1.811
1-19	7 a.m.	I-35S	0.000	32,456.021	1.490

Date	Hour	Driving Direction	Nugget	Range (m)	Sill
1-19	9 a.m.	I-35N	0.107	20,479.940	1.171
1-19	9 a.m.	I-35S	0.023	23,550.910	0.988
1-22	11 a.m.	I-35N	0.023	38,979.604	0.042
1-22	2 p.m.	I-35N	0.000	8,954.332	0.050
1-22	2 p.m.	I-35S	0.000	18,763.525	0.104
1-22	3 p.m.	I-35N	0.000	34,298.760	0.299
1-22	3 p.m.	I-35S	0.049	56,863.120	0.132
1-22	4 p.m.	I-35N	0.016	15,624.883	0.060
1-22	4 p.m.	I-35S	0.095	258.424	0.108
1-22	5 p.m.	I-35N	0.000	12,648.146	0.366
1-22	6 p.m.	I-35S	0.045	23,143.331	0.493
1-22	7 p.m.	I-35N	0.000	26,761.321	1.007
1-22	8 p.m.	I-35S	0.000	22,494.843	0.884
1-22	9 p.m.	I-35N	0.000	33,031.344	1.244
1-22	10 p.m.	I-35S	0.000	25,461.301	1.589
1-22	7 a.m.	I-35N	0.000	25,966.869	0.451
1-22	7 a.m.	I-35S	0.028	17,815.955	0.187
1-22	8 a.m.	I-35N	0.083	364.085	0.094
1-22	8 a.m.	I-35S	0.000	28,703.004	0.292
1-22	9 a.m.	I-35S	0.032	5,3367.243	0.045
1-23	0 a.m.	I-35S	0.010	12,915.149	0.610
1-23	1 a.m.	I-35S	0.067	35,987.972	0.459
1-23	2 a.m.	I-35N	0.276	1,812.654	0.355
1-23	3 a.m.	I-35N	0.000	19,866.694	1.387
1-23	3 a.m.	I-35S	0.000	13,883.415	0.506
1-23	4 a.m.	I-35S	0.282	54,478.743	0.670
1-23	6 a.m.	I-35N	0.000	24,380.660	1.062
1-23	6 a.m.	I-35S	0.000	56,404.708	2.333
1-23	8 a.m.	I-35N	0.299	18,887.605	0.588
1-23	8 a.m.	I-35S	0.000	6,412.863	0.510
1-23	9 a.m.	I-35N	0.275	57,127.195	1.238
2-4	1 p.m.	I-35S	0.279	8,583.810	0.404
2-5	2 p.m.	I-35N	0.210	52,972.533	0.230
2-5	3 p.m.	I-35S	0.016	20,960.062	0.848
2-5	4 p.m.	I-35N	0.193	56,562.711	1.376
2-5	4 p.m.	I-35S	0.084	54,911.166	0.557
2-6	12 p.m.	I-35S	0.390	55,817.658	0.390
2-6	1 p.m.	I-35N	0.070	61,412.866	0.529

Date	Hour	Driving Direction	Nugget	Range (m)	Sill
3-7	10 a.m.	I-35N	0.120	29,561.928	0.400
3-7	10 a.m.	I-35S	0.301	390.661	0.414
3-7	8 a.m.	I-35S	0.102	18,140.169	0.334
4-22	10 a.m.	I-35S	0.371	35,804.614	0.732

Table A-3. All cross validation results for RST

Date	Hour	Driving Direction	RMSE (1RWIS)	RMSE (2RWIS)	RMSE (3RWIS)	$\overline{\sigma^2}$ (1RWIS)	$\overline{\sigma^2}$ (2RWIS)	$\overline{\sigma^2}$ (3RWIS)
2018								
10-26	12 p.m.	I-35S	1.398	1.268	1.201	0.285	0.278	0.276
11-7	1 p.m.	I-35N	1.399	1.147	1.003	3.519	2.639	1.415
11-8	10 a.m.	I-35N	0.601	0.805	0.624	0.933	0.700	0.562
11-8	10 a.m.	I-35S	0.733	0.865	0.599	0.139	0.131	0.128
11-8	11 a.m.	I-35S	0.617	0.691	0.579	0.211	0.191	0.184
11-8	9 p.m.	I-35S	1.115	0.582	0.529	0.135	0.127	0.124
11-8	8 a.m.	I-35N	1.547	0.862	0.615	0.302	0.226	0.000
11-8	9 a.m.	I-35N	0.714	0.593	0.532	0.593	0.445	0.395
11-8	9 a.m.	I-35S	1.034	0.927	0.746	0.226	0.214	0.210
11-9	10 a.m.	I-35N	0.859	0.697	0.597	0.972	0.756	0.602
11-9	9 a.m.	I-35N	0.733	0.718	0.670	0.966	0.725	0.522
11-9	9 a.m.	I-35S	0.644	0.693	0.851	0.052	0.051	0.051
11-17	11 a.m.	I-35N	0.424	0.247	0.215	0.113	0.085	0.071
11-17	12 p.m.	I-35S	0.319	0.319	0.319	0.062	0.057	0.055
11-17	1 p.m.	I-35N	0.318	0.729	0.547	0.218	0.164	0.119
11-17	1 p.m.	I-35S	0.171	0.226	0.153	0.022	0.019	0.019
11-17	2 p.m.	I-35N	0.228	0.378	0.324	0.089	0.067	0.057
11-17	2 p.m.	I-35S	0.197	0.308	0.236	0.016	0.015	0.014
11-17	3 p.m.	I-35N	0.121	0.130	0.113	0.025	0.018	0.016
11-17	3 p.m.	I-35S	0.291	0.405	0.322	0.018	0.017	0.017
11-17	4 p.m.	I-35N	0.375	0.236	0.237	0.139	0.104	0.068
11-17	4 p.m.	I-35S	0.341	0.186	0.188	0.027	0.025	0.025
11-17	5 p.m.	I-35N	0.269	0.368	0.327	0.143	0.107	0.038
11-17	5 p.m.	I-35S	0.488	0.379	0.365	0.141	0.125	0.119
11-17	6 p.m.	I-35N	0.495	0.474	0.463	0.497	0.372	0.320
11-17	6 p.m.	I-35S	0.971	1.361	0.870	0.185	0.163	0.156
11-17	7 p.m.	I-35N	1.545	0.686	0.686	0.514	0.385	0.340

Date	Hour	Driving Direction	RMSE (1RWIS)	RMSE (2RWIS)	RMSE (3RWIS)	$\overline{\sigma^2}$ (1RWIS)	$\overline{\sigma^2}$ (2RWIS)	$\overline{\sigma^2}$ (3RWIS)
11-17	7 p.m.	I-35S	0.566	0.745	0.680	0.027	0.026	0.026
11-17	8 p.m.	I-35N	0.549	0.545	0.471	0.623	0.467	0.376
11-17	8 p.m.	I-35S	0.862	0.639	0.518	0.071	0.070	0.069
11-17	9 p.m.	I-35S	0.523	0.511	0.504	0.044	0.043	0.043
11-17	10 p.m.	I-35N	0.678	0.650	0.833	0.909	0.681	0.566
11-17	10 p.m.	I-35S	0.746	0.681	0.623	0.323	0.299	0.289
11-17	11 p.m.	I-35N	0.873	0.849	0.671	2.251	1.688	1.030
11-17	11 p.m.	I-35S	0.951	0.602	0.587	0.051	0.050	0.050
11-18	1 a.m.	I-35N	0.484	0.449	0.453	0.423	0.317	0.282
11-18	2 a.m.	I-35S	0.515	0.449	0.445	0.262	0.230	0.219
11-18	3 a.m.	I-35N	0.396	0.377	0.396	0.369	0.277	0.220
11-18	3 a.m.	I-35S	1.424	0.889	0.809	0.480	0.385	0.354
11-18	4 a.m.	I-35N	0.414	0.823	0.918	0.332	0.249	0.213
11-18	4 a.m.	I-35S	0.383	0.523	0.346	0.089	0.080	0.077
11-18	5 a.m.	I-35S	0.682	0.826	1.252	0.081	0.079	0.078
11-18	6 a.m.	I-35N	0.424	0.492	0.456	0.444	0.333	0.291
11-25	10 a.m.	I-35N	0.540	0.598	0.465	0.334	0.251	0.213
11-25	10 a.m.	I-35S	0.398	0.486	0.313	0.042	0.036	0.034
11-25	12 p.m.	I-35N	0.838	0.683	0.735	0.869	0.714	0.000
11-25	12 p.m.	I-35S	0.539	0.452	0.313	0.188	0.150	0.140
11-25	1 p.m.	I-35N	0.403	0.403	0.401	0.355	0.267	0.237
11-25	1 p.m.	I-35S	0.940	0.663	0.488	0.080	0.078	0.077
11-25	2 p.m.	I-35N	0.489	0.464	0.406	0.381	0.287	0.232
11-25	2 p.m.	I-35S	0.745	0.541	0.521	0.023	0.023	0.023
11-25	3 p.m.	I-35S	0.536	0.465	0.585	0.137	0.128	0.125
11-25	4 p.m.	I-35N	0.901	0.750	1.035	1.488	1.116	0.957
11-25	5 p.m.	I-35S	0.620	0.585	0.535	0.026	0.025	0.025
11-25	6 p.m.	I-35N	0.805	0.713	0.592	1.022	0.767	0.638
11-25	6 p.m.	I-35S	0.536	0.697	0.540	0.318	0.270	0.256
11-25	7 p.m.	I-35N	0.640	0.802	0.733	0.786	0.590	0.498
11-25	7 p.m.	I-35S	0.500	0.516	0.708	0.237	0.217	0.210
11-25	8 p.m.	I-35S	0.708	0.626	0.725	0.074	0.071	0.070
11-25	9 p.m.	I-35S	1.010	0.519	0.633	0.070	0.068	0.068
11-25	10 p.m.	I-35N	0.630	0.567	0.577	0.689	0.517	0.436
11-25	6 a.m.	I-35N	0.447	0.613	0.593	0.314	0.235	0.182
11-25	6 a.m.	I-35S	0.417	0.426	0.376	0.237	0.074	0.072
11-25	7 a.m.	I-35N	0.261	0.242	0.237	0.100	0.075	0.063
11-25	7 a.m.	I-35S	0.146	0.109	0.128	0.019	0.015	0.013

Date	Hour	Driving Direction	RMSE (1RWIS)	RMSE (2RWIS)	RMSE (3RWIS)	$\overline{\sigma^2}$ (1RWIS)	$\overline{\sigma^2}$ (2RWIS)	$\overline{\sigma^2}$ (3RWIS)
11-25	8 a.m.	I-35N	0.199	0.309	0.238	0.082	0.061	0.054
11-25	8 a.m.	I-35S	0.217	0.267	0.229	0.031	0.029	0.028
11-25	9 a.m.	I-35N	0.462	0.370	0.363	0.379	0.284	0.252
11-25	9 a.m.	I-35S	0.234	0.306	0.243	0.011	0.011	0.011
11-26	0 a.m.	I-35S	0.832	0.898	1.147	0.386	0.352	0.340
11-26	11 a.m.	I-35N	1.471	1.136	1.087	3.698	2.775	2.240
11-26	11 a.m.	I-35S	0.773	0.808	0.796	0.405	0.373	0.363
11-26	12 p.m.	I-35N	1.633	1.469	1.508	3.266	2.450	2.177
11-26	12 p.m.	I-35S	1.218	1.328	1.040	0.152	0.150	0.150
11-26	2 p.m.	I-35N	0.874	1.019	0.975	1.941	1.456	0.954
11-26	4 a.m.	I-35N	1.221	0.839	0.902	1.223	0.917	0.812
11-26	6 a.m.	I-35N	0.550	0.399	0.391	0.512	0.384	0.294
11-26	8 a.m.	I-35S	1.121	1.267	1.182	1.616	1.319	1.220
11-27	11 a.m.	I-35N	1.737	1.305	1.012	1.788	1.343	0.972
12-3	11 a.m.	I-35S	0.371	0.370	0.378	0.163	0.138	0.130
12-4	10 p.m.	I-35N	0.363	0.381	0.361	0.241	0.181	0.000
12-4	10 p.m.	I-35S	0.407	0.358	0.344	0.063	0.059	0.057
12-4	7 a.m.	I-35N	0.396	0.396	0.421	0.338	0.253	0.000
12-4	7 a.m.	I-35S	0.401	0.486	0.452	0.349	0.222	0.204
12-7	8 a.m.	I-35N	1.168	0.814	0.795	1.235	0.927	0.000
12-12	10 a.m.	I-35S	1.018	1.179	0.946	0.567	0.504	0.483
12-12	2 p.m.	I-35S	0.952	0.808	0.850	0.759	0.648	0.612
12-12	8 a.m.	I-35N	0.268	0.193	0.150	0.101	0.077	0.000
12-19	9 a.m.	I-35S	0.505	0.490	0.501	0.032	0.032	0.032
12-24	8 a.m.	I-35N	0.624	0.610	0.610	0.982	0.737	0.614
12-24	8 a.m.	I-35S	0.900	1.000	0.615	0.092	0.088	0.087
12-24	9 a.m.	I-35S	2.418	0.973	0.694	0.363	0.233	0.227
12-28	5 a.m.	I-35N	0.987	0.650	0.627	0.674	0.505	0.000
12-28	6 a.m.	I-35N	0.617	0.567	0.540	0.695	0.521	0.463
12-28	6 a.m.	I-35S	0.481	0.489	0.486	0.124	0.117	0.114
12-28	7 a.m.	I-35N	1.716	0.772	0.825	1.294	0.971	0.379
12-28	7 a.m.	I-35S	0.610	0.577	0.664	0.014	0.014	0.014
12-31	1 p.m.	I-35S	0.253	0.265	0.247	0.087	0.072	0.066
12-31	2 p.m.	I-35N	0.281	0.280	0.307	0.156	0.117	0.102
12-31	2 p.m.	I-35S	0.499	0.480	0.467	0.027	0.027	0.026
12-31	3 p.m.	I-35N	0.371	0.286	0.290	0.101	0.076	0.063
12-31	3 p.m.	I-35S	0.417	0.340	0.328	0.205	0.157	0.140
12-31	4 p.m.	I-35S	0.278	0.275	0.290	0.066	0.058	0.055

Date	Hour	Driving Direction	RMSE (1RWIS)	RMSE (2RWIS)	RMSE (3RWIS)	$\overline{\sigma^2}$ (1RWIS)	$\overline{\sigma^2}$ (2RWIS)	$\overline{\sigma^2}$ (3RWIS)
2019								
1-11	6 p.m.	I-35N	0.411	0.325	0.268	0.053	0.040	0.035
1-11	6 p.m.	I-35S	0.151	0.164	0.158	0.034	0.027	0.024
1-11	7 p.m.	I-35N	0.088	0.140	0.105	0.010	0.008	0.007
1-11	7 p.m.	I-35S	0.061	0.100	0.077	0.006	0.004	0.004
1-11	8 p.m.	I-35N	0.007	0.007	0.007	0.001	0.000	0.000
1-11	8 p.m.	I-35S	0.206	0.153	0.190	0.003	0.003	0.003
1-11	9 p.m.	I-35N	0.160	0.154	0.563	0.047	0.035	0.031
1-11	9 p.m.	I-35S	0.463	0.263	0.192	0.001	0.001	0.001
1-11	10 p.m.	I-35N	0.283	0.150	0.109	0.008	0.006	0.005
1-11	10 p.m.	I-35S	0.114	0.078	0.073	0.010	0.007	0.007
1-11	8 a.m.	I-35S	0.305	0.248	0.286	0.127	0.000	0.000
1-12	0 a.m.	I-35N	0.422	0.566	0.462	0.495	0.371	0.308
1-12	0 a.m.	I-35S	0.547	0.373	0.704	0.016	0.016	0.016
1-12	10 a.m.	I-35N	0.310	0.265	0.498	0.140	0.107	0.000
1-12	10 a.m.	I-35S	0.283	0.229	0.238	0.008	0.008	0.008
1-12	11 a.m.	I-35N	0.080	0.076	0.205	0.009	0.007	0.000
1-12	12 p.m.	I-35S	0.748	0.412	0.327	0.008	0.008	0.008
1-12	2 p.m.	I-35N	0.765	0.653	0.576	0.818	0.615	0.409
1-12	2 p.m.	I-35S	0.680	0.530	0.530	0.052	0.051	0.051
1-12	3 p.m.	I-35N	0.572	0.442	0.456	0.910	0.693	0.404
1-12	4 p.m.	I-35N	0.202	0.260	0.251	0.112	0.084	0.041
1-12	4 p.m.	I-35S	0.250	0.253	0.253	0.049	0.045	0.043
1-12	5 p.m.	I-35N	0.063	0.063	0.102	0.007	0.005	0.004
1-12	5 p.m.	I-35S	0.362	0.376	0.373	0.012	0.011	0.011
1-12	6 p.m.	I-35S	0.542	0.532	0.533	0.024	0.023	0.023
1-12	7 p.m.	I-35N	0.446	0.393	0.396	0.340	0.259	0.172
1-12	7 p.m.	I-35S	0.391	0.341	0.371	0.048	0.045	0.044
1-12	1 a.m.	I-35N	0.385	0.356	0.345	0.253	0.189	0.168
1-12	1 a.m.	I-35S	0.698	0.554	0.380	0.040	0.039	0.039
1-12	8 p.m.	I-35N	0.423	0.384	0.375	0.329	0.247	0.165
1-12	8 p.m.	I-35S	0.241	0.182	0.161	0.029	0.025	0.024
1-12	9 p.m.	I-35N	0.285	0.183	0.178	0.073	0.055	0.047
1-12	9 p.m.	I-35S	0.208	0.177	0.177	0.021	0.020	0.019
1-12	2 a.m.	I-35N	0.486	0.325	0.314	0.266	0.199	0.163
1-12	2 a.m.	I-35S	0.526	0.593	0.441	0.219	0.189	0.177
1-12	3 a.m.	I-35N	0.383	0.360	0.383	0.328	0.246	0.192
1-12	3 a.m.	I-35S	0.394	0.540	0.481	0.071	0.067	0.066

Date	Hour	Driving Direction	RMSE (1RWIS)	RMSE (2RWIS)	RMSE (3RWIS)	$\overline{\sigma^2}$ (1RWIS)	$\overline{\sigma^2}$ (2RWIS)	$\overline{\sigma^2}$ (3RWIS)
1-12	4 a.m.	I-35N	0.478	0.577	0.530	0.526	0.395	0.348
1-12	4 a.m.	I-35S	0.952	0.575	0.476	0.117	0.111	0.109
1-12	5 a.m.	I-35N	1.087	0.655	0.718	0.721	0.541	0.415
1-12	5 a.m.	I-35S	1.031	0.663	0.591	0.031	0.031	0.031
1-12	6 a.m.	I-35N	0.483	0.425	0.434	0.462	0.346	0.205
1-12	6 a.m.	I-35S	0.584	0.547	0.511	0.113	0.108	0.107
1-12	7 a.m.	I-35S	0.486	0.482	0.522	0.478	0.358	0.319
1-12	8 a.m.	I-35N	0.479	0.433	0.431	0.399	0.299	0.263
1-12	9 a.m.	I-35N	0.462	0.437	0.494	0.318	0.239	0.204
1-12	9 a.m.	I-35S	0.396	0.319	0.305	0.082	0.075	0.072
1-14	9 p.m.	I-35S	0.025	0.025	0.025	0.002	0.001	0.001
1-14	10 p.m.	I-35S	0.014	0.014	0.014	0.001	0.001	0.001
1-15	7 a.m.	I-35N	0.061	0.037	0.109	0.001	0.001	0.000
1-15	7 a.m.	I-35S	0.028	0.028	0.033	0.002	0.001	0.001
1-15	8 a.m.	I-35N	0.141	0.158	0.154	0.032	0.024	0.000
1-17	10 a.m.	I-35S	1.722	0.882	0.557	0.060	0.059	0.059
1-17	9 a.m.	I-35N	0.171	0.147	0.163	0.047	0.035	0.030
1-17	9 a.m.	I-35S	0.299	0.307	0.386	0.104	0.085	0.078
1-18	3 p.m.	I-35N	0.557	0.505	0.516	0.473	0.355	0.316
1-18	3 p.m.	I-35S	0.520	0.491	0.498	0.132	0.124	0.121
1-18	4 p.m.	I-35N	0.720	0.664	0.628	0.708	0.531	0.453
1-18	4 p.m.	I-35S	0.737	0.439	0.509	0.326	0.260	0.235
1-18	5 p.m.	I-35N	0.685	0.591	0.599	0.586	0.439	0.349
1-18	5 p.m.	I-35S	0.806	0.545	0.495	0.278	0.247	0.237
1-18	6 p.m.	I-35N	0.821	0.849	0.840	1.138	0.854	0.072
1-18	6 p.m.	I-35S	0.665	0.658	0.693	0.112	0.110	0.109
1-18	7 p.m.	I-35N	0.879	0.590	0.589	0.900	0.675	0.565
1-18	8 p.m.	I-35N	0.892	0.905	0.906	1.987	1.490	1.106
1-18	8 p.m.	I-35S	1.298	0.998	0.993	0.052	0.051	0.051
1-18	9 p.m.	I-35N	1.105	0.679	0.643	0.817	0.613	0.545
1-18	10 p.m.	I-35S	0.817	0.859	0.835	0.060	0.059	0.059
1-18	11 p.m.	I-35N	0.997	0.778	0.481	1.355	1.016	0.613
1-19	0 a.m.	I-35N	1.414	1.272	1.239	2.083	1.562	1.364
1-19	0 a.m.	I-35S	1.170	1.112	0.901	0.062	0.062	0.062
1-19	11 a.m.	I-35S	3.069	2.810	1.701	2.047	1.952	1.948
1-19	1 p.m.	I-35S	1.099	3.196	2.164	1.371	1.174	1.097
1-19	1 a.m.	I-35N	1.205	0.816	0.806	1.296	0.972	0.864
1-19	1 a.m.	I-35S	0.764	0.759	1.024	0.575	0.497	0.464

Date	Hour	Driving Direction	RMSE (1RWIS)	RMSE (2RWIS)	RMSE (3RWIS)	$\overline{\sigma^2}$ (1RWIS)	$\overline{\sigma^2}$ (2RWIS)	$\overline{\sigma^2}$ (3RWIS)
1-19	2 a.m.	I-35N	0.812	0.785	0.707	0.756	0.574	0.000
1-19	3 a.m.	I-35N	1.443	1.660	1.573	2.767	2.075	1.828
1-19	3 a.m.	I-35S	0.676	0.666	0.632	0.478	0.399	0.366
1-19	4 a.m.	I-35N	1.377	1.109	1.027	2.387	1.790	1.536
1-19	5 a.m.	I-35S	0.817	0.630	0.606	0.041	0.040	0.040
1-19	6 a.m.	I-35N	1.316	2.427	1.821	2.950	2.212	1.838
1-19	7 a.m.	I-35N	1.250	1.371	1.342	3.506	2.667	2.078
1-19	7 a.m.	I-35S	1.386	1.282	1.197	0.076	0.076	0.075
1-19	9 a.m.	I-35N	1.197	1.333	1.363	2.343	1.757	0.419
1-19	9 a.m.	I-35S	1.253	1.141	1.679	0.114	0.112	0.112
1-22	11 a.m.	I-35N	0.240	0.188	0.184	0.085	0.063	0.055
1-22	2 p.m.	I-35N	0.243	0.286	0.334	0.100	0.075	0.067
1-22	2 p.m.	I-35S	0.361	0.360	0.365	0.009	0.009	0.009
1-22	3 p.m.	I-35N	0.595	0.520	0.517	0.599	0.449	0.338
1-22	3 p.m.	I-35S	0.488	0.570	0.523	0.100	0.091	0.086
1-22	4 p.m.	I-35N	0.331	0.272	0.337	0.121	0.091	0.081
1-22	4 p.m.	I-35S	0.409	0.428	0.382	0.217	0.163	0.145
1-22	5 p.m.	I-35N	0.766	0.747	0.726	0.732	0.549	0.487
1-22	6 p.m.	I-35S	0.803	0.632	0.640	0.122	0.119	0.117
1-22	7 p.m.	I-35N	1.418	0.793	0.787	2.013	1.510	1.262
1-22	8 p.m.	I-35S	1.013	0.852	0.791	0.065	0.065	0.064
1-22	9 p.m.	I-35N	1.534	0.920	0.615	2.489	1.866	1.430
1-22	10 p.m.	I-35S	1.334	1.143	0.849	0.103	0.103	0.102
1-22	7 a.m.	I-35N	0.642	0.574	0.554	0.901	0.676	0.571
1-22	7 a.m.	I-35S	0.419	0.427	0.397	0.071	0.067	0.066
1-22	8 a.m.	I-35N	0.371	0.395	0.363	0.187	0.141	0.125
1-22	8 a.m.	I-35S	0.659	0.400	0.396	0.017	0.017	0.017
1-22	9 a.m.	I-35S	0.327	0.280	0.269	0.065	0.053	0.049
1-23	0 a.m.	I-35S	0.733	0.737	0.793	0.096	0.094	0.094
1-23	1 a.m.	I-35S	0.772	0.684	0.622	0.152	0.146	0.144
1-23	2 a.m.	I-35N	1.003	0.577	0.609	0.710	0.532	0.473
1-23	3 a.m.	I-35N	1.335	1.305	1.315	2.774	2.080	1.848
1-23	3 a.m.	I-35S	1.126	1.042	0.814	0.060	0.060	0.059
1-23	4 a.m.	I-35S	0.822	0.775	0.763	0.577	0.515	0.488
1-23	6 a.m.	I-35N	0.975	1.499	0.884	2.125	1.594	1.370
1-23	6 a.m.	I-35S	1.660	1.337	1.380	0.069	0.068	0.068
1-23	8 a.m.	I-35N	0.745	0.899	0.816	1.176	0.882	0.784
1-23	8 a.m.	I-35S	0.793	0.799	0.873	0.132	0.127	0.126

Date	Hour	Driving Direction	RMSE (1RWIS)	RMSE (2RWIS)	RMSE (3RWIS)	$\overline{\sigma^2}$ (1RWIS)	$\overline{\sigma^2}$ (2RWIS)	$\overline{\sigma^2}$ (3RWIS)
1-23	9 a.m.	I-35N	1.310	1.490	0.839	2.446	1.842	1.246
2-4	1 p.m.	I-35S	0.812	0.631	0.838	0.582	0.477	0.442
2-5	2 p.m.	I-35N	0.555	1.049	0.761	0.460	0.345	0.301
2-5	3 p.m.	I-35S	1.018	2.164	1.686	0.097	0.096	0.095
2-5	4 p.m.	I-35N	1.593	0.983	0.984	2.520	1.943	0.902
2-5	4 p.m.	I-35S	0.699	0.897	0.840	0.183	0.175	0.172
2-6	12 p.m.	I-35S	1.121	1.318	1.128	0.779	0.584	0.519
2-6	1 p.m.	I-35N	0.948	0.815	0.829	1.022	0.778	0.478
3-7	10 a.m.	I-35N	0.714	0.715	0.666	0.799	0.600	0.499
3-7	10 a.m.	I-35S	0.942	0.906	0.780	0.827	0.621	0.552
3-7	8 a.m.	I-35S	0.735	0.581	0.579	0.226	0.207	0.200
4-22	10 a.m.	I-35S	0.832	0.887	0.777	0.759	0.661	0.613

APPENDIX B. RESULTS OF SPATIAL MAPPING OF ROAD SURFACE INDEX

Note that the following tables summarize the corresponding results involved in the steps of spatial mapping of RSI, including fitting a trend model for RSI, semivariogram model parameters and cross validation results.

Table B-1. Fitted trend models involved in RK for RSI in 2019

Date	Hour	Driving Direction	Significant variables	Sign of coefficients	R ²
1-12	1 a.m.	I-35N	Altitude/altitude ²	(+)/(-)	32%
1-12	4 a.m.	I-35N	NA	NA	NA
1-12	8 a.m.	I-35N	Altitude	(-)	21%
1-19	0 a.m.	I-35N	Altitude	(-)	14%
1-19	1 a.m.	I-35N	NA	NA	NA
1-22	7 p.m.	I-35N	NA	NA	NA
1-22	8 p.m.	I-35N	NA	NA	NA
1-22	9 p.m.	I-35N	Altitude/altitude ²	(-)/(-)	32%
1-22	8 a.m.	I-35N	NA	NA	NA
1-23	4 a.m.	I-35N	Latitude	(-)	25%
2-12	1 a.m.	I-35N	NA	NA	NA
2-17	8 a.m.	I-35N	Latitude/slope/latitude ² /slope ²	(-)/(-)/(-)/(-)	19%
2-20	1 a.m.	I-35N	Altitude/altitude ²	(+)/(+)	20%
2-20	2 a.m.	I-35N	Altitude/altitude ²	(-)/(-)	13%
2-20	3 a.m.	I-35N	NA	NA	NA
2-23	9 p.m.	I-35N	Latitude	(-)	12%
2-24	0 a.m.	I-35N	Latitude	(-)	9%
2-24	1 a.m.	I-35N	Latitude/latitude ²	(-)/(-)	10%
2-24	3 a.m.	I-35N	NA	NA	NA
3-7	8 a.m.	I-35N	NA	NA	NA
3-7	9 a.m.	I-35N	NA	NA	NA
11-25	10 a.m.	I-35S	Altitude/altitude ²	(+)/(+)	56%
1-12	1 a.m.	I-35S	NA	NA	NA
1-18	8 p.m.	I-35S	Altitude/altitude ²	(-)/(-)	37%
1-19	3 a.m.	I-35S	NA	NA	NA
1-22	8 p.m.	I-35S	NA	NA	NA
1-22	10 p.m.	I-35S	NA	NA	NA
1-28	0 a.m.	I-35S	Latitude	(-)	9%
2-10	8 a.m.	I-35S	NA	NA	NA
2-11	9 p.m.	I-35S	Altitude/altitude ²	(-)/(-)	9%
2-12	2 a.m.	I-35S	NA	NA	NA
2-17	1 a.m.	I-35S	Latitude/slope	(-)/(-)	50%

Date	Hour	Driving Direction	Significant variables	Sign of coefficients	R ²
2-20	4 a.m.	I-35S	Latitude	(-)	19%

Table B-2. Fitted semivariogram models for RSI in 2019

Date	Hour	Driving Direction	Nugget	Range (m)	Sill
1-12	1 a.m.	I-35N	0.010	30,676.037	0.018
1-12	4 a.m.	I-35N	0.016	47,126.735	0.034
1-12	8 a.m.	I-35N	0.007	35,581.762	0.015
1-19	0 a.m.	I-35N	0.013	51,378.292	0.024
1-19	1 a.m.	I-35N	0.017	60,843.049	0.017
1-22	7 p.m.	I-35N	0.024	61,051.271	0.024
1-22	8 p.m.	I-35N	0.015	9,102.644	0.023
1-22	9 p.m.	I-35N	0.010	55,335.794	0.010
1-22	8 a.m.	I-35N	0.003	42,898.411	0.006
1-23	4 a.m.	I-35N	0.015	13,754.682	0.021
2-12	1 a.m.	I-35N	0.010	46,720.326	0.014
2-17	8 a.m.	I-35N	0.012	61,343.116	0.012
2-20	1 a.m.	I-35N	0.015	54,917.779	0.017
2-20	2 a.m.	I-35N	0.017	20,462.764	0.022
2-20	3 a.m.	I-35N	0.020	1,310.306	0.020
2-23	9 p.m.	I-35N	0.006	19,748.756	0.006
2-24	0 a.m.	I-35N	0.017	44,722.581	0.017
2-24	1 a.m.	I-35N	0.011	60,839.910	0.011
2-24	3 a.m.	I-35N	0.008	15,603.060	0.011
3-7	8 a.m.	I-35N	0.007	8,735.845	0.011
3-7	9 a.m.	I-35N	0.003	54,858.401	0.009
11-25	10 a.m.	I-35S	0.019	52,330.546	0.019
1-12	1 a.m.	I-35S	0.004	19,175.416	0.022
1-18	8 p.m.	I-35S	0.009	55,272.873	0.009
1-19	3 a.m.	I-35S	0.007	51,577.888	0.014
1-22	8 p.m.	I-35S	0.019	55,291.390	0.019
1-22	10 p.m.	I-35S	0.009	53,170.563	0.013
1-28	0 a.m.	I-35S	0.005	52,922.557	0.005
2-10	8 a.m.	I-35S	0.001	53,575.737	0.001
2-11	9 p.m.	I-35S	0.021	52,991.753	0.021
2-12	2 a.m.	I-35S	0.009	51,991.032	0.011
2-17	1 a.m.	I-35S	0.003	40,266.124	0.016

Date	Hour	Driving Direction	Nugget	Range (m)	Sill
2-20	4 a.m.	I-35S	0.016	55,318.410	0.016

Table B-3. All cross validation results for RSI in 2019

Date	Hour	Driving Direction	RMSE (1RWIS)	RMSE (2RWIS)	RMSE (3RWIS)	$\overline{\sigma^2}$ (1RWIS)	$\overline{\sigma^2}$ (2RWIS)	$\overline{\sigma^2}$ (3RWIS)
1-12	1 a.m.	I-35N	0.160	0.158	0.179	0.036	0.027	0.023
1-12	4 a.m.	I-35N	0.193	0.196	0.208	0.068	0.051	0.040
1-12	8 a.m.	I-35N	0.140	0.128	0.116	0.030	0.022	0.018
1-19	0 a.m.	I-35N	0.147	0.201	0.146	0.044	0.034	0.000
1-19	1 a.m.	I-35N	0.156	0.135	0.135	0.033	0.025	0.022
1-22	7 p.m.	I-35N	0.234	0.234	0.156	0.048	0.036	0.032
1-22	8 p.m.	I-35N	0.199	0.199	0.199	0.046	0.035	0.031
1-22	9 p.m.	I-35N	0.102	0.102	0.102	0.020	0.015	0.014
1-22	8 a.m.	I-35N	0.081	0.081	0.171	0.012	0.009	0.007
1-23	4 a.m.	I-35N	0.192	0.141	0.158	0.042	0.031	0.028
2-12	1 a.m.	I-35N	0.155	0.117	0.117	0.028	0.021	0.016
2-17	8 a.m.	I-35N	0.113	0.113	0.108	0.023	0.017	0.015
2-20	1 a.m.	I-35N	0.134	0.130	0.134	0.033	0.025	0.021
2-20	2 a.m.	I-35N	0.152	0.145	0.143	0.043	0.033	0.029
2-20	3 a.m.	I-35N	0.168	0.136	0.138	0.039	0.029	0.026
2-23	9 p.m.	I-35N	0.077	0.085	0.078	0.012	0.009	0.000
2-24	0 a.m.	I-35N	0.144	0.184	0.153	0.033	0.025	0.000
2-24	1 a.m.	I-35N	0.107	0.110	0.118	0.022	0.017	0.015
2-24	3 a.m.	I-35N	0.122	0.170	0.115	0.022	0.017	0.015
3-7	8 a.m.	I-35N	0.103	0.104	0.102	0.022	0.017	0.015
3-7	9 a.m.	I-35N	0.094	0.098	0.090	0.018	0.014	0.008
11-25	10 a.m.	I-35S	0.151	0.152	0.146	0.038	0.000	0.000
1-12	1 a.m.	I-35S	0.142	0.184	0.182	0.045	0.023	0.022
1-18	8 p.m.	I-35S	0.100	0.154	0.132	0.017	0.013	0.012
1-19	3 a.m.	I-35S	0.190	0.133	0.102	0.028	0.000	0.000
1-22	8 p.m.	I-35S	0.189	0.189	0.139	0.038	0.028	0.025
1-22	10 p.m.	I-35S	0.123	0.123	0.123	0.018	0.015	0.013
1-28	0 a.m.	I-35S	0.073	0.079	0.074	0.010	0.007	0.007
2-10	8 a.m.	I-35S	0.028	0.028	0.028	0.002	0.001	0.001
2-11	9 p.m.	I-35S	0.154	0.151	0.158	0.042	0.032	0.028
2-12	2 a.m.	I-35S	0.132	0.113	0.132	0.017	0.014	0.013

Date	Hour	Driving Direction	RMSE (1RWIS)	RMSE (2RWIS)	RMSE (3RWIS)	$\overline{\sigma^2}$ (1RWIS)	$\overline{\sigma^2}$ (2RWIS)	$\overline{\sigma^2}$ (3RWIS)
2-17	1 a.m.	I-35S	0.215	0.153	0.195	0.032	0.007	0.007
2-20	4 a.m.	I-35S	0.169	0.125	0.126	0.033	0.024	0.022

**THE INSTITUTE FOR TRANSPORTATION IS THE FOCAL POINT FOR TRANSPORTATION
AT IOWA STATE UNIVERSITY.**

InTrans centers and programs perform transportation research and provide technology transfer services for government agencies and private companies;

InTrans contributes to Iowa State University and the College of Engineering's educational programs for transportation students and provides K–12 outreach; and

InTrans conducts local, regional, and national transportation services and continuing education programs.



**IOWA STATE
UNIVERSITY**

Visit InTrans.iastate.edu for color pdfs of this and other research reports.